

PAPER • OPEN ACCESS

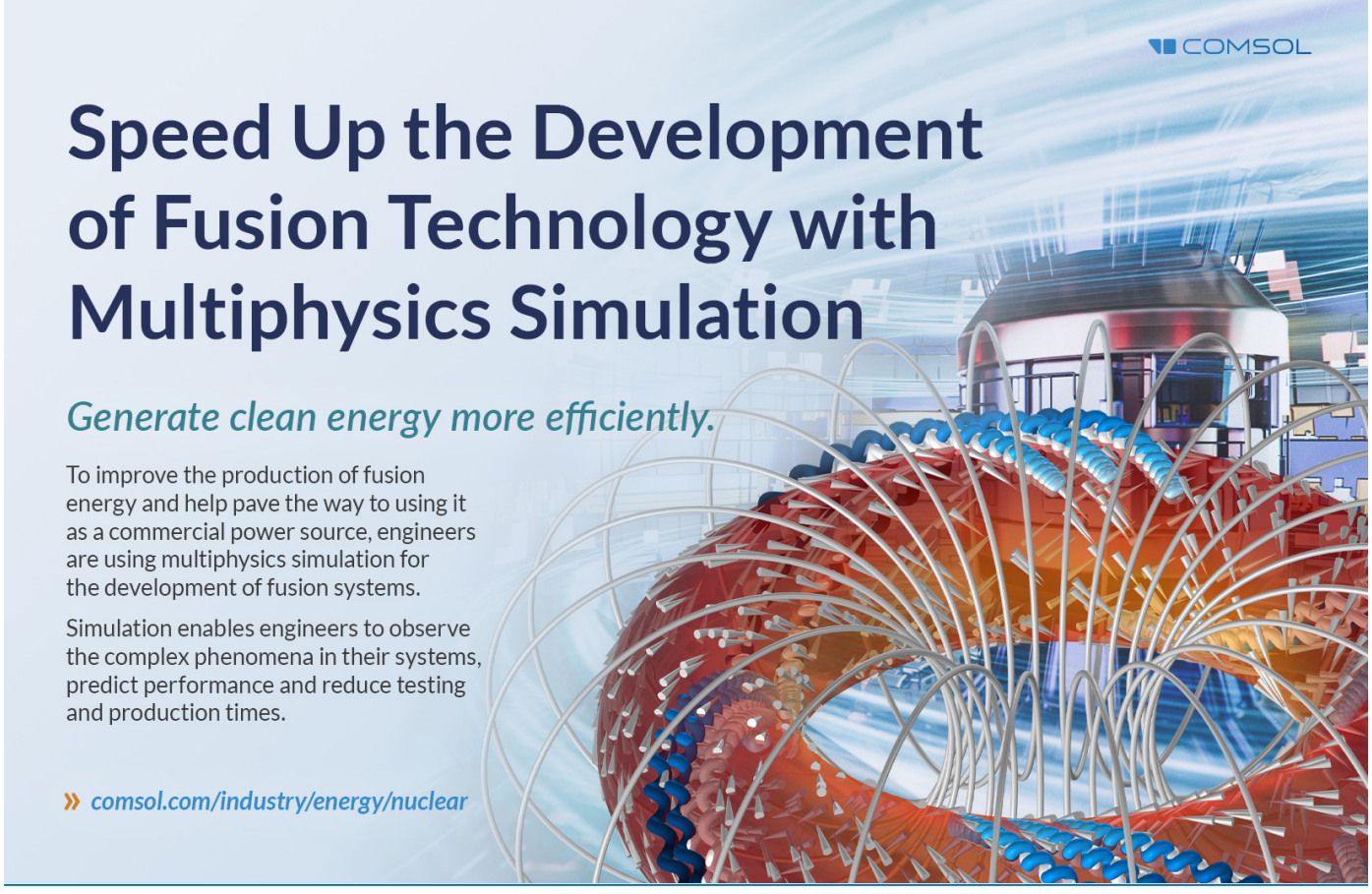
Simulation and analysis of a high-*k* electron-scale turbulence diagnostic for MAST-U

To cite this article: D.C. Speirs et al 2025 Nucl. Fusion 65 046019

View the article online for updates and enhancements.

You may also like

- Transport and confinement physics: Chapter 2 of the special issue: on the path to tokamak burning plasma operation M. Yoshida, R.M. McDermott, C. Angioni et al.
- Experimental characteristics of lost fast negative ions on EAST tokamak
 Z.X. Zhang, J. Huang, J.F. Chang et al.
- Experimental research on the TCV tokamak
 B.P. Duval, A. Abdolmaleki, M. Agostini et al.



Nucl. Fusion 65 (2025) 046019 (21pp)

https://doi.org/10.1088/1741-4326/adb761

Simulation and analysis of a high-k electron-scale turbulence diagnostic for MAST-U

D.C. Speirs^{1,*}, J. Ruiz Ruiz², M. Giacomin^{3,4}, V.H. Hall-Chen⁵, A.D.R. Phelps¹, R. Vann⁴, P.G. Huggard⁶, H. Wang⁶, A. Field⁷ and K. Ronald¹

E-mail: david.c.speirs@strath.ac.uk

Received 20 August 2024, revised 10 January 2025 Accepted for publication 18 February 2025 Published 20 March 2025



Abstract

Plasma turbulence on disparate spatial and temporal scales plays a key role in defining the level of confinement achievable in tokamaks, with the development of reduced numerical models for cross-scale turbulence effects informed by experimental measurements an essential step. MAST-U is a well-equipped facility having instruments to measure ion and electron scale turbulence at the plasma edge. However, measurement of core electron scale turbulence is challenging, especially in H mode. Using a novel synthetic diagnostic approach, we present simulated measurement specifications of a proposed highly optimised mm-wave based collective scattering instrument for measuring both normal and bi-normal electron scale turbulence in the core and edge of MAST-U. A powerful modelling framework has been developed that combines beam-tracing techniques with gyrokinetic simulations to predict the sensitivity and spectral range of measurement, with a quasi-numerical approach used to analyse the corresponding instrument selectivity functions. For the reconstructed MAST 022769 shot, a maximum measurable normalised bi-normal wavenumber of $k_{\perp} \rho_{e} \sim 0.6$ was predicted in the core and $k_{\perp} \rho_e \sim 0.79$ near the pedestal, with localisation lengths $L_{\rm FWHM}$ ranging from ~ 0.4 m in the core at k_{\perp} $\rho_e \sim 0.1$ to ~ 0.08 m at k_{\perp} $\rho_e > 0.45$. Synthetic diagnostic analysis for the 022769 shot using CGYRO gyrokinetic simulation spectra reveal that electron temperature

^{*} Author to whom any correspondence should be addressed.



Original content from this work may be used under the terms of the Creative Commons Attribution 4.0 licence. Any fur-

ther distribution of this work must maintain attribution to the author(s) and the title of the work, journal citation and DOI.

¹ Department of Physics, SUPA, University of Strathclyde, Glasgow G4 0NG, United Kingdom of Great Britain and Northern Ireland

² Rudolf Peierls Centre for Theoretical Physics, University of Oxford, Oxford OX1 3NP, United Kingdom of Great Britain and Northern Ireland

³ Dipartimento di Fisica 'G. Galilei', Università degli Studi di Padova, Padova, Italy

⁴ York Plasma Institute, Department of Physics, University of York, Heslington, York YO10 5DD, United Kingdom of Great Britain and Northern Ireland

⁵ Institute of High Performance Computing, Agency for Science, Technology, and Research (A*STAR), Singapore 138632, Singapore

⁶ Millimetre Wave Technology Group, RAL Space, STFC Rutherford Appleton Laboratory, Didcot OX11 0QX, United Kingdom of Great Britain and Northern Ireland

⁷ United Kingdom Atomic Energy Authority, Culham, United Kingdom of Great Britain and Northern Ireland

gradient turbulence wavenumbers of peak spectral intensity comfortably fall within the measurable/detectable range of the instrument from the core to the pedestal. The proposed diagnostic opens up opportunities to study new regimes of turbulence and confinement, particularly in association with upcoming non-inductive, microwave based current drive experiments on MAST-U and can provide insight into cross-scale turbulence effects, while having suitability to operate during burning plasma scenarios on future reactors such as Spherical Tokamak for Energy Production.

Keywords: plasma, turbulence, scattering, gyrokinetic simulation

(Some figures may appear in colour only in the online journal)

1. Introduction

1.1. Motivation

Heat transport, due to turbulence on the scale of the electron Larmor radius, is important in defining the confinement and consequent fusion performance of spherical aspect ratio tokamak plasmas [1-3]. In a tokamak, nested flux surfaces are formed by toroidal and poloidal magnetic fields. These surfaces permit relatively free transport of particles and energy along the lines of flux ψ but limit cross-field transport in the radial direction². This facilitates the development of a hot dense plasma core, with an energy confinement time long enough for ions and electrons to reach thermal equilibrium and temperatures sufficient for a sustainable fusion reaction [4]. Minimising cross-field transport is key to achieving the required plasma conditions. Turbulence dominates cross-field transport losses [1, 5]. Turbulent eddies exist at scales extending from the electron Larmor radius to the ion Larmor radius and macroscopic structures approaching the machine size. Although significant progress has been made in understanding the mechanisms and drivers of turbulent transport in plasma [1, 6-8], complex feedback mechanisms coupling the interaction of these eddies across many orders of magnitude in space and time make predictive modelling extremely challenging [9, 10]. Detailed experimental data at both electron and ion scales is therefore required to formulate the reduced models necessary to develop schemes that minimise turbulent cross-field transport.

Spherical aspect-ratio tokamaks, such as MAST-U at the Culham Centre for Fusion Energy (CCFE), offer a potential path to compact fusion power [11]. Theoretical predictions suggest that spherical tokamaks may benefit from enhanced confinement compared to larger, conventional aspect-ratio tokamaks [3], with some authors inferring a near-linear scaling in confinement time with toroidal magnetic field [11]. This enhanced confinement is believed to be due to more extreme toroidicity and larger $E \times B$ shearing rates on spherical tokamaks, both of which can supress electrostatic drift wave instabilities and turbulence at both ion and electron scales. Predictions of transport from discrete ion and electron scale simulations, however, do not always match experimental observations [12]. Numerically challenging cross-scale simulations, resolving both ion and electron contributions, reveal

that the electron scale can indirectly enhance ion scale turbulence by disrupting sub ion-scale flows [9, 10]. This can lead to an order of magnitude increase in cross-field transport at the ion scale, significantly reducing confinement and the viability of achieving fusion ignition and burn in a spherical tokamak. With recent significant investments announced by governments [13–16] and private industry [11] to develop tokamak based fusion powerplants, the urgency to understand cross-scale turbulent interactions has never been greater, with experimental measurements of electron and ion scale turbulence in the core plasma essential for model development. On MAST-U, the beam emission spectroscopy (BES) diagnostic can measure ion scale turbulence in the core plasma [17]. The UCLA [18] and SWIP [19] DBS (Doppler back-scattering) diagnostics on MAST-U can measure intermediate to electronscale turbulence up to $k_{\perp}\rho_s \sim 9 \ (k_{\perp}\rho_e \sim 0.15)$ where $\rho_s =$ $\sqrt{m_i T_i/(qB)}$ is the ion (deuterium) sound radius and ρ_e the electron gyroradius, but have limited core accessibility (constrained to lower density operational regimes) and a measurement location and spatial localisation that is dependent on the cut-off surface location and gradient profile. We have therefore developed a novel, mm-wavelength coherent scattering diagnostic for MAST-U that can measure high-k (large wavenumber) electron scale turbulence under all operating conditions of the experimental reactor.

1.2. Proposed high-k scattering instrument

Spatial anisotropy has been observed in electron temperature gradient (ETG) driven turbulence which helps motivate the orientation/alignment of measurement for the high-k scattering diagnostic [20–22]. ETG electron scale turbulence is expected to be most significant in the bi-normal direction, i.e. perpendicular to the magnetic field and in-plane with the flux surface. Scale ranges are expected to be of order $k_{\perp}\rho_{e} \sim 0.1->0.4$ [23] in the confinement region of the core plasma (0.5 < r/a < 1) where k_{\perp} is the wavenumber of the turbulence, r is the tokamak minor radial coordinate and a is the tokamak minor radius. Previous multiscale simulations have been conducted by Maeyama $et\ al\ [9,\ 10]$ for the so-called Cyclone DIII-D base case (density and temperature gradient ratio $L_n/L_{T_i}=L_n/L_{T_e}=3.1$, temperature ratio $T_i/T_e=1$, magnetic shear $\hat{s}=0.78$, safety factor q=1.4 and aspect ratio

 $R_m/a = 5.6$ where R_m is the tokamak major radius). These predict turbulence growth rates peaking at $k_{\perp}\rho_{s}\approx0.45$ and $k_{\perp}\rho_{s}\approx 18~(k_{\perp}\rho_{e}~\approx 0.3)$ for ion and electron scales respectively under $\beta = 2\mu_0 (n_i T_i + n_e T_e) / B^2 = 0.04\%$ and 2% with μ_0 the vacuum permittivity, n_i and n_e the ion and electron number densities and using a realistic ion-electron mass ratio $m_i/m_e = 1836$. In order to validate numerical predictions, it is essential to measure turbulence at both ion and electron scales within the core and edge plasma. MAST-U provides an optimum opportunity to make such measurements using the BES and proposed high-k scattering diagnostics. These measurements will be of particular high value on MAST-U, where a dual frequency electron Bernstein wave (EBW) heating and current drive system is scheduled for installation in 2025 [24]. Understanding the impact that different EBW and neutralbeam current-drive configurations have on plasma flow and associated confinement on MAST-U will be critical, and the ability to monitor variations in electron and ion scale turbulent transport within the core plasma will be of key importance for theory and model development.

The principle of a high-k scattering diagnostic is that part of a collimated electromagnetic wave is scattered at an angle given by the vector sum of its wavevector and that of the turbulence, with a Doppler shift in frequency due to the movement of the turbulent eddies: see figure 1. Measurement of the deflected signal amplitude as a function of scattering angle allows the turbulence spectrum to be mapped in wavevector space, identifying the dominant scale lengths. Given an electron Larmor radius in MAST-U of ~0.2 mm, the implied turbulence wavelength range is of order a few mm. The scattering wavevector resolution scales as the reciprocal of the beam waist $(1/e^2)$ intensity radius at the measurement location, which is set to be of order \sim 2 cm. To measure unambiguously the scattered signals requires that they are spatially separated from the probe beam, and each other, by more than the beam width at the detector location. The probe beam frequency is set by a number of criteria: (1) it should be greater than twice the maximum prevailing plasma frequency to ensure unfettered access to the plasma volume with minimal effect of refraction on the beam path, (2) it should not be so high that the deflection associated with the turbulence wavevector range of interest would not present clearly separated beams, (3) adequately powerful sources and sensitive detectors are available and (4) it should not be at a harmonic of the frequencies of the MAST-U high power EBW heating gyrotrons, at 28 GHz and 34.8 GHz. This all points to a frequency in the range 330-400 GHz. The practical choice is 376 GHz, which takes advantage of the availability of 94 GHz transistor power amplifiers for radar applications when frequency multiplied by four, i.e. two successive stages of frequency multiplication can be used deliver a 376 GHz beam.

The proposed instrument will be novel in several ways, with an illustration of the projected scattering geometry and installation across the MAST-U vessel given in figure 2. Other high-*k* diagnostics have been implemented, with great success, in particular a system developed by University of California, Davis (UCD) for NSTX [25, 26] and a new system being developed by UCD for NSTX-U [27]. The UCD system deployed on

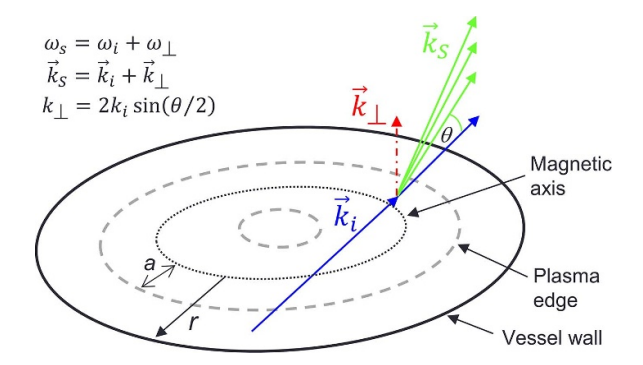


Figure 1. Proposed bi-normal high-k scattering geometry across MAST-U plasma. An equatorial plain representation shows the incident wavevector k_i , turbulence wavevector k_\perp and scattered wavevector k_s along with three-wave matching and Bragg condition in terms of scattering angle θ .

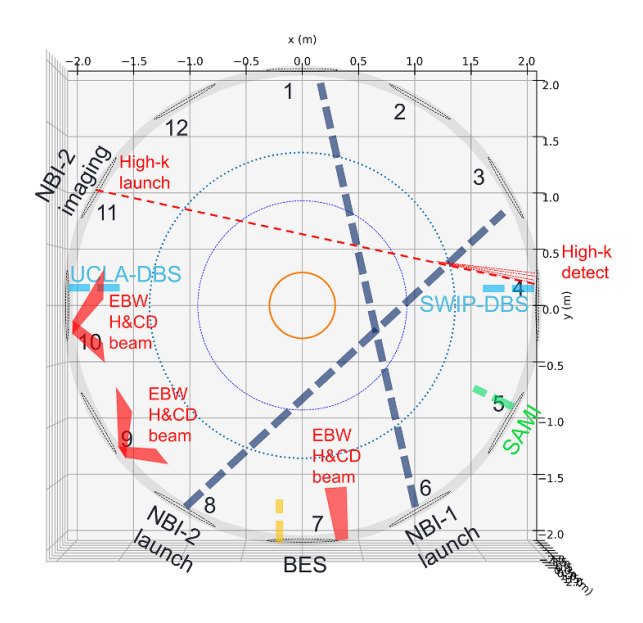


Figure 2. Proposed bi-normal high-*k* scattering geometry and installation across MAST-U vessel. Other key systems and diagnostics are illustrated for [17–19].

NSTX used a vacuum tube source and was configured for radial scattering. The proposed system for NSTX-U will focus on bi-normal scattering and will use a frequency >600 GHz from a molecular vapour laser. To make our system highly deployable we propose to use solid state multiplication of high frequency, high power, solid state sources to a sub-mm frequency of 376 GHz, exploiting a rapidly developing field of enabling technologies. These sources are largely unaffected by the magnetic fields of a tokamak, resulting in closer proximity to the vacuum vessel and lower transmission loss. We have designed a predominantly reflective optical system, thereby avoiding dielectric loss and standing wave problems. Entrance and exit windows will be of low hydroxyl fused quartz with minimum absorption and a thickness tuned for Fabry–Perot resonant transmission.

A particularly innovative feature is that the linear array of detectors will rotate to track the bi-normal direction for all plausible tokamak equilibria at a range of radial scattering

locations from the axis to the pedestal. This will (a) minimise the number of tokamak shots required to map the turbulence and (b) more importantly, allow simultaneous measurements using all bi-normally aligned channels to reveal temporal correlations—this is anticipated to allow deeper scientific study of the coupling across the electron scale turbulence spectrum. A further capability of the proposed diagnostic is the ability to measure both bi-normal and normal (perpendicular to the magnetic field, perpendicular to the flux surface) oriented turbulence. This can be achieved by off-setting the rotational pitch of the carriage from strictly bi-normal. Each channel will then be in alignment with a combination of binormal and normal scattering contributions. The precise ratio and magnitude of these contributions can be computed for a given equilibrium via beam tracing. Results of simulations presented later in this paper demonstrate this.

2. Theory

2.1. Collective scattering

The scattering of microwaves by density fluctuations in plasma has already proven a valuable method for diagnosing fusion plasma turbulence [18, 26]. Such scattering can be termed coherent (collective) if the turbulence wavelength is of the order of or much greater than the Debye length in the plasma $\lambda_{\rm De} = \sqrt{(\epsilon_0 k_{\rm B} T_e/n_e e^2)}$, where $k_{\rm B}$ is Boltzmann constant, ϵ_0 is the vacuum permittivity, T_e is the electron temperature, n_e is the electron density and e is the electron charge. In a coherent scattering regime, the scattered waves are representative of the collective electron motion manifesting as fluctuations in the refractive index. The total scattered power for a plane wave scattered by a single coherent density fluctuation is given by the classical formula [25]

$$P_s = \frac{1}{4} P_i r_e^2 L_{\text{FWHM}}^2 \lambda_i^2 \delta n_e^2 \tag{1}$$

where λ_i is the incident beam wavelength, P_i is the incident beam power, L_{FWHM} is the spatial resolution (full-width halfmaximum overlap of scattered and incident beams enhanced by magnetic field pitch rotation with radius), r_e is the classical electron radius and δn_e is the density modulation amplitude. This formula makes no assumption about the anisotropy of a density fluctuation spectrum and provides an estimate of the minimum density fluctuation power that can be detected. In strongly magnetised plasmas, the spectrum of the turbulence is anisotropic in the parallel and perpendicular directions with respect to the background magnetic field. The turbulence exhibits length scales perpendicular to the magnetic field that are much smaller than along the field. The turbulence fluctuations are commonly described by a wavevector k_{\perp} perpendicular to the field, while its component $k_{||}$ is small, $k_{||} \ll k_{\perp}$, consistent with the ordering in the turbulence theory of gyrokinetics [28, 29]. This means that in order to measure electron-scale fluctuations using high-k scattering, one needs to carefully design the launching and receiving apparatus in such a way that the incident and scattered rays not only intersect, but they do so while satisfying the condition that the difference between the scattered and incident beam wavenumbers at the scattering location, $\mathbf{k}_s - \mathbf{k}_i$, lies on the perpendicular plane to the magnetic field [30]. We call this difference the measured, or selected, turbulence wavenumber $\mathbf{k}_{\perp} = \mathbf{k}_s - \mathbf{k}_i$. In this manuscript, we have designed the incident and scattered beams such that this condition is satisfied for all the selected wavenumbers shown. We are particularly interested in the scattering of a microwave beam of radius w_b from a turbulent, anisotropic density fluctuation spectrum $\delta \hat{n}_e(\mathbf{k},\omega)$. A more appropriate formula for the scattered power over an angular aperture of π $(2/k_i w_b^2)$ for such a density fluctuation spectrum can be estimated by [31]

$$P_{s} = P_{i} \frac{k_{i}^{2} L_{\text{FWHM}}^{2}}{k_{i}^{2} w_{b}^{2}} \frac{\omega_{pe}^{4}}{\omega_{i}^{4}} \left(\frac{\delta n_{e}^{2}}{n_{e}^{2}}\right)_{\text{rms}}$$
(2)

where $\omega_{pe} = \left(n_e e^2/m_e \epsilon_0\right)^{\frac{1}{2}}$ is the electron plasma frequency, ω_i is the incident angular frequency, $k_i = \omega_i/c$ is the incident wavenumber of the microwave beam, $k_{\perp} = |\boldsymbol{k}_i - \boldsymbol{k}_s|$ is the magnitude of the selected scattered wavenumber of the turbulence, and $(\delta n_e/n_e)_{\rm rms}^2$ is the root mean square of the turbulence fluctuation power. Equation (2) will be used in this manuscript to calculate the threshold $(\delta n_e/n_e)_{\rm rms}^2$ that can be detectable by the diagnostic. Details of the derivation can be found in [28]. Note that in equation (2), the only unknown is the spatial resolution $L_{\rm FWHM}$. An estimate of the diagnostic spatial resolution is given next.

Using an analysis following that of Mazzucato [32], one can obtain the instrument selectivity function for the receiving detector channel. We consider the beam spectrum $G(\kappa_{\perp}) = \exp\left(-\kappa_{\perp}^2/\Delta^2\right)$ where $\Delta = 2/w_b$ (assuming we are scattering from the beam waist) and κ_{\perp} is the wavenumber perpendicular to the direction of propagation of the channel matched wavevector k_{S1} , which satisfies the scattering condition that $k_{S1} - k_i$ remains perpendicular to the local magnetic field B. This ensures that the scattered beam of wave vector k_{S1} arrives at the detector with maximal efficiency.

In the proposed diagnostic, the detector and receiving optics have angular adjustment to ensure that bi-normal alignment is met for k_{S1} at the selected scattering coordinate. A beam of central wave vector k_{Sm} originating from the same scattering location however will result in $k_{Sm} - k_i$ having a component along B. Therefore, k_{Sm} will be mismatched with respect to k_{S1} , and the scattered amplitude arriving at the detector will be attenuated by the mismatch. This property has been extensively used in the past to localise high-k scattering measurements [30, 32] as well as more recently in DBS [33-35] while k_{Sm} is the mismatched wavevector (see figure 3). In what follows, we closely follow Mazzucato [32, 36] and use the property of the mismatched wave vectors to arrive at an expression for the instrument selectivity function F. We start by calculating the projection of the mismatched scattered wavevector in the perpendicular plane κ_{\perp} of the matched wavevector

$$\boldsymbol{\kappa}_{\perp Sm} = \boldsymbol{k}_{Sm} - (\boldsymbol{k}_{Sm} \cdot \hat{\boldsymbol{s}}_1) \hat{\boldsymbol{s}}_1$$

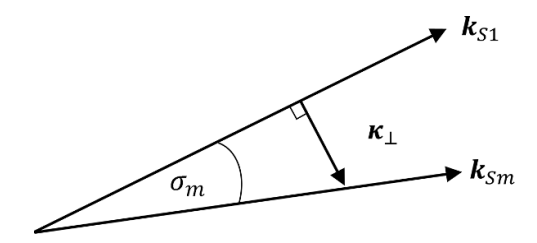


Figure 3. Matched k_{S1} and mismatched k_{Sm} scattered beam wavevectors with mismatch angle σ_m .

After squaring both sides and some vector algebra we get

$$\boldsymbol{\kappa}_{\perp Sm}^2 = \boldsymbol{k}_{Sm}^2 \left(1 - (\hat{\boldsymbol{s}}_1 \cdot \hat{\boldsymbol{s}}_m)^2 \right)$$

where \hat{s}_1 and \hat{s}_m are the unit vectors for the matched and mismatched scattered beams respectively and $\hat{s}_1 \cdot \hat{s}_m = \cos \sigma_m = \frac{k_{S1} \cdot k_{Sm}}{|k_{S1}| |k_{Sm}|}$. Substituting into the equation for the beam spectrum $G(\kappa_\perp)$ we have

$$F = G(\boldsymbol{\kappa}_{\perp Sm}) = \exp\left(\frac{-k_i^2}{\Delta^2} \left(1 - \left(\frac{\boldsymbol{k}_{S1} \cdot \boldsymbol{k}_{Sm}}{|\boldsymbol{k}_{S1}| |\boldsymbol{k}_{Sm}|}\right)^2\right)\right)$$
(3)

where F is the instrument selectivity function, which can be analysed via a quasi-numerical approach using the projected wavevectors of mismatched scattered beams. The mismatch is due to magnetic field pitch rotation relative to the value at the scattering coordinate, resulting in rotational misalignment of the scattered beam with respected to matched incidence.

Another fundamental limit on the instrument localisation of measurement is the projection of the Gaussian scattered beam intensity relative to the primary beam—the so-called 'beam overlap'. The impact of this is illustrated in figure 4 and has been previously analysed for a collective Thomson scattering diagnostic [37].

With reference to figure 4, the Gaussian beam waist overlap is maximum at an angle of $\theta/2$ to the primary and scattered beams, yielding an overlap waist of $w_b/\sin(\theta/2)$ and an instrument selectivity envelope of

$$F_{\text{Gauss}}(L) = \exp\left(-\left(\frac{L\Delta\sin\left(\theta/2\right)}{2}\right)^{2}\right). \tag{4}$$

Combined with the mismatch instrument selectivity function in (3), we have a resultant instrument selectivity function of

$$F(L) = \exp\left(\frac{-k_i^2}{\Delta^2} \left(1 - \left(\frac{\mathbf{k}_{S1} \cdot \mathbf{k}_{Sm}}{|\mathbf{k}_{S1}| |\mathbf{k}_{Sm}|}\right)^2\right) - \left(\frac{L\Delta \sin\left(\theta/2\right)}{2}\right)^2\right). \tag{5}$$

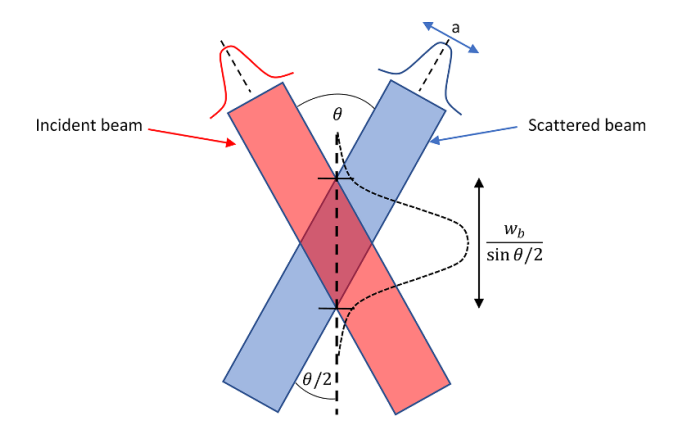


Figure 4. Illustration of incident and scattered Gaussian beam overlap along coordinate L, with the $1/e^2$ scattered beam waist projected at $\theta/2$ to the incident beam, where θ is the scattering angle, yielding an effective $1/e^2$ overlap radius of $w_b/\sin(\theta/2)$.

The first term in the exponential of equation (5) governs the localisation effect due to variation in magnetic field pitch angle rotation with radius, whilst the second term accounts for the incident and scattered Gaussian beam overlap region as a function of scattering angle $\theta/2$. From equation (5) the spatial localisation length $L_{\rm FWHM}$ can be estimated by taking the FWHM of the resultant peak profile centred around the scattering coordinate. This will provide a quantitative assessment of the minimum scattered power detectable by the diagnostic for a given $\delta n_{e_{\rm rms}}^2$. The spatial resolution $L_{\rm FWHM}$ will also be used in a synthetic high-k diagnostic to quantitatively predict the scattered power spectrum.

The selected k_{\perp} is routinely decomposed into its components in the directions normal and bi-normal to the background magnetic field $B = B \hat{\mathbf{b}}$, where $\hat{\mathbf{b}}$ is the unit vector along the background magnetic field and B is its magnitude. The normal direction to the flux surface is directed along the normal unit vector $\hat{\mathbf{e}}_{\mathbf{n}} = \frac{\nabla \psi}{|\nabla \psi|}$, where $\nabla \psi$ is the gradient of the flux function. The bi-normal direction is directed along the bi-normal unit vector $\hat{\mathbf{e}}_{\mathbf{b}} = \hat{\mathbf{e}}_{\mathbf{n}} \times \hat{\mathbf{b}}$. Using these definitions, we define the normal and bi-normal wavenumber components of the selected wavevector k_{\perp} by $k_{\perp} = k_n \hat{\mathbf{e}}_{\mathbf{n}} + k_b \hat{\mathbf{e}}_{\mathbf{b}}$. The normal and bi-normal wavenumber components of the turbulence will be used in section 3.4 to implement a synthetic diagnostic for high-k scattering.

2.2. Beam tracing of primary and scattered waves

The beam tracing code Scotty [35] has been used to compute the primary and scattered ray trajectories (receiving window aperture limited) as a function of radius for a variety of MAST-U operational equilibria. Scotty is a beam tracing code written entirely in Python 3 using cylindrical polar coordinates $(R, \zeta, Z,)$ natively. This simplifies the beam tracing equations by exploiting the toroidal symmetry of tokamaks. Scotty assumes lossless propagation and was executed without

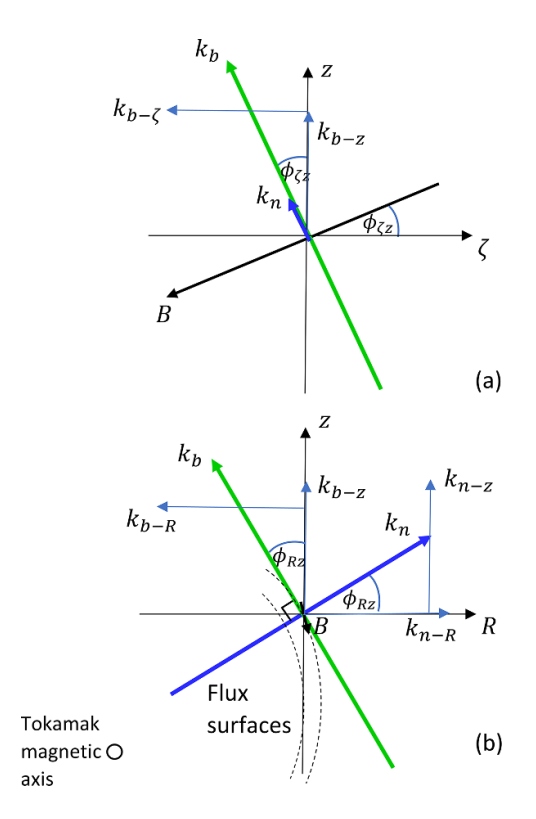


Figure 5. Scattering wavenumber projections in cylindrical polar coordinates for (a) R–z and (b) ζ –z planes.

relativistic corrections to the electron mass, a mode suitable for lower temperature devices such as MAST-U.

Scotty solves the beam tracing equations for the primary ray trajectory, projecting from the launching port to the receiving port, through the plasma. Scattered ray trajectories are then computed for an array of prescribed bi-normal k_b and normal k_n turbulence wavenumbers. Looking at figure 5, the turbulence wavevector projections are presented in cylindrical polar coordinates in R-z and $\zeta-z$ planes along with the magnetic field vector \mathbf{B} , where ζ is the toroidal coordinate, R is the radial coordinate and z is the vertical coordinate (perpendicular to the equatorial plane). The angles ϕ_{Rz} and $\phi_{\zeta z}$ are respectively the R-z and $\zeta-z$ angles of the magnetic field at a given scattering coordinate in the plasma.

Scotty solves the beam tracing equations for the primary ray trajectory, projecting from the launching port to the receiving port, through the plasma. Scattered ray trajectories are then computed for an array of prescribed bi-normal k_b and normal k_n turbulence wavenumbers. Looking at figure 5, the turbulence wavevector projections are presented in cylindrical polar coordinates in R-z and $\zeta-z$ planes along with the magnetic field vector \mathbf{B} , where ζ is the toroidal coordinate, R is the radial coordinate and z is the vertical coordinate (perpendicular to the equatorial plane). The angles ϕ_{Rz} and $\phi_{\zeta z}$ are respectively the R-z and $\zeta-z$ angles of the magnetic field at a given scattering coordinate in the plasma. As the scattering wavenumber $k_s = k_i + k_\perp$ where k_i is the incident beam wavenumber and k_\perp is the turbulence wavenumber, the contributions of k_b and

 k_n must be calculated in cylindrical polar coordinates, k_R , k_ζ and k_z , subject to the angular rotations ϕ_{Rz} and $\phi_{\zeta z}$. This yields the following set of scattering equations in k_n and k_b

$$k_{R} = k_{R_{p}} + S_{b} \sin \phi_{Rz} k_{b} + S_{n} \cos \phi_{Rz} k_{n}$$

$$k_{\zeta} = k_{\zeta_{p}} + S_{b} \sin \phi_{\zeta z} \cos \phi_{Rz} k_{b} - S_{n} \sin \phi_{\zeta z} \sin \phi_{Rz} k_{n}$$

$$k_{z} = k_{z_{p}} + S_{b} \cos \phi_{\zeta z} \cos \phi_{Rz} k_{b} - S_{n} \cos \phi_{\zeta z} \sin \phi_{Rz} k_{n}$$
 (6)

where k_{ζ} is negative for clockwise toroidal rotation and positive for counter-clockwise toroidal rotation in Scotty (viewed from above), k_R is positive for radially outwards components and negative for radially inwards components and k_z is positive for upwards (above midplane) components and negative for downwards (below midplane) components. The parameter $S_n = 1$ is the scattering sign (direction) for k_n and $S_b = -1$ is the scattering sign (direction) for k_b .

Looking at figure 6, one can see the resultant scattered component distribution for a predefined range in k_b and k_n . The primary ray is illustrated in red, the green scattered components represent strictly bi-normal scattering from $k_b = 3.98 \times 10^2 \rightarrow 1.78 \times 10^3 \text{ m}^{-1}$, whilst the blue scattered components correspond to a $k_b = 3.98 \times 10^2 \text{ m}^{-1}$ and $k_n = 8.75 \times 10^2 \rightarrow 3.5 \times 10^3 \text{ m}^{-1}$. The arrows indicate the respective directions of the magnetic field, bi-normal and normal wavevectors.

3. Results and analysis

3.1. Optical component configuration

The optical component configuration of the launching and receiving carriages for the proposed high-k diagnostic is now considered via ABCD matrix analysis [38]. The proposed high-k scattering instrument comprises a 376 GHz Gaussian beam launched across the MAST-U vacuum vessel between opposing equatorial ports, at near perpendicular incidence to the magnetic field and toroidal coordinate at the plasma outboard pedestal. The Gaussian beam divergence and $1/e^2$ radius is controlled to ensure a flat beam waist region of \sim 2 cm from the magnetic axis to the outboard plasma pedestal, closest to the receiving window. This facilitates adjustment of the scattering radius over the full depth of the plasma and normalised radial range of $r/a = 0 \rightarrow 1$, whilst maintaining a constant $1/e^2$ radius. A projection of the beam waist evolution is given in figure 7 from an ABCD matrix code. One spherical focussing mirror with $R_{c1} = 0.635$ m is employed to focus the divergent beam following the launching antenna, with a planar 2-axis adjustable steering mirror inserted prior to traversing the vacuum vessel wall. At the receiving end, a focussingdefocussing mirror pair with radii of curvature $R_{c2} = 0.80 \text{ m}$ and $R_{c3} = -0.60$ m respectively is used to focus and redirect the beam into the detector array with a $1/e^2$ waist radius $w_b \approx 0.8$ cm.

An illustration of the launching optics carriage is presented in figure 8. This will be mounted 0.16 m above midplane, horizontally aligned on a 600 mm equatorial port flange, utilising a 120 mm diameter low hydroxyl fused silica window for

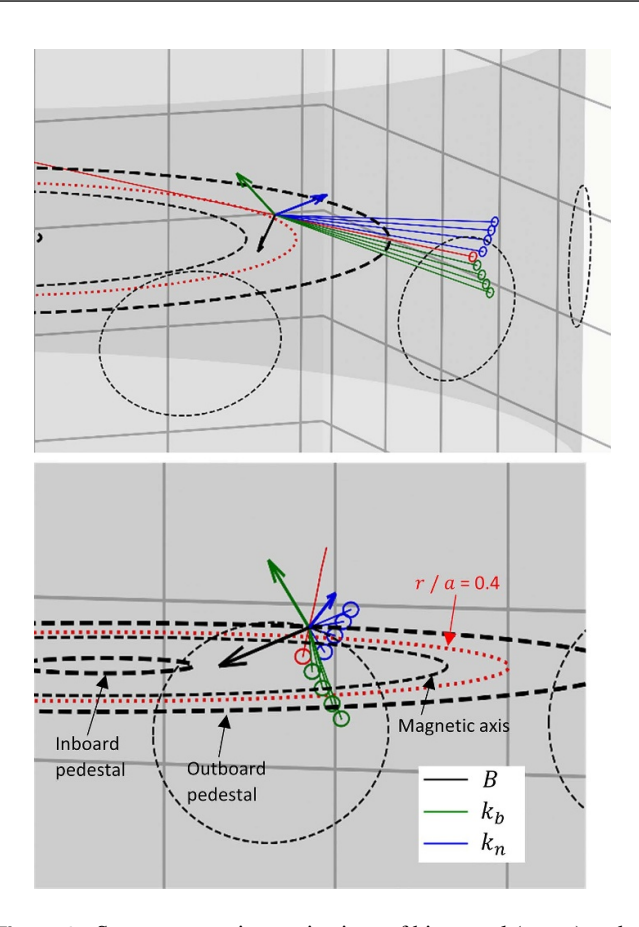


Figure 6. Scotty ray-tracing projections of bi-normal (green) and normal (blue) turbulence scattering from a reference beam (red). The scattered spectrum turbulence wavenumbers are $k_n = 0$, $k_b = 3.98 \times 10^2$, 8.59×10^2 , 1.32×10^3 , $1.78 \times 10^3 \text{m}^{-1}$ (green) and $k_b = 3.98 \times 10^2 \text{m}^{-1}$, $k_n = 8.75 \times 10^2$, 1.75×10^3 , 2.63×10^3 , $3.5 \times 10^3 \text{m}^{-1}$ (blue).

minimum transmission losses on entry into the vacuum vessel. A rotatable linear polariser will facilitate precise polarisation control of the launched beam. The detection optics carriage is illustrated in figure 7. The receiving optics will collect the primary and scattered beams via a 250 mm × 290 mm elliptical window, also fabricated from low OH content fused silica. The thickness of this window will be tuned for maximum Fabry–Perot resonant transmission corresponding to the wavenumber with lowest scattered power (largest scattering angle), maximising the signal to noise ratio for the weakest signals. The entire assembly within the receiving carriage is mounted on a linear translation stage, allowing the focus of the receiving optics, i.e. the scattering volume, to be scanned in radius via a motorised linear drive.

A separate rotational stage facilitates rotation of the receiving optics assembly and linearly aligned detector channel array. This rotation is centred around the primary ray, enabling alignment to be maintained with the poloidal scattering direction dictated by the pitch angle of the magnetic field, which varies as a function of radius and under different operational equilibria. A linear polariser is also mounted on entry into the

receiving optics carriage. This can be independently rotated to facilitate co and cross-polar detection of the scattered radiation, allowing detection of both density and magnetic fluctuations within the scattering volume.

The blue dashed lines in the lower-right quadrant of figure 9 indicate the positions of the upper and lower P5 poloidal field coils in MAST-U. The position of the elliptical receiving window and path of the scattered rays has been optimised to ensure no interception of scattered components on the P5 coils or their mounting brackets.

3.2. Ray tracing simulations of the scattered spectrum and analysis of the instrument selectivity function

The beam tracing code Scotty [35] has been used in ray tracing mode to predict the aperture limited primary and scattered beam paths for the high-k diagnostic as a function of scattering radius and operational equilibrium on MAST-U. The diametrically opposing ports on MAST-U have been selected for this analysis due to their optimal positioning to achieve a primary beam path projected across the plasma that is nearperpendicular to the magnetic field and outer pedestal over the scattering region, while avoiding tangential propagation near the inner pedestal earlier in the trajectory that would result in greater refraction of the primary beam path. Figure 10 shows the primary and scattered ray propagation paths for a sample high-beta MAST-U equilibrium (see appendix) with an aperture limited 4 channel scattered component distribution for three radial scattering coordinates. The ray trajectories are shown in figure 10(a), with the corresponding magnetic field pitch angle rotations in $\zeta - z$ and r - z plotted as a function of radius and the scattering coordinate values highlighted.

The maximum $k_{\perp}\rho_e$ values measurable for each scattering radius (aperture limited) are shown, with a maximum $k_{\perp}\rho_e$ of 0.43 at $R_{\rm scatt}=1.24$ m. Figure 10(b) shows the localisation length of the scattering region as a function of $k_{\perp}\rho_e$ scattering radius. The localisation lengths $L_{\rm FWHM}$ are the FWHM of the instrument selectivity functions plotted in figure 10(c) which are generated using equation (5), showing the overlap of the scattered and incident Gaussian beam envelopes [37] constrained by the pitch rotation of the magnetic field [36] along the beam overlap length L (at $\theta/2$ to the primary and scattered rays). The localisation length has an upper limit corresponding to the last closed flux surface at R=1.3 m.

Figure 11 shows the receiving window (aperture limited) 4 channel scattered component distributions for the 022769 MAST shot [39]. There are four radial scattering coordinates used in this case, corresponding to r/a = 0.4, 0.5, 0.6 and 0.8. The scattering data from these simulations is used in the synthetic diagnostic analysis that follows in section 3.4, using the results of gyrokinetic simulations of ETG turbulence for the corresponding r/a values outlined in section 3.3 below. Due to the lower magnetic field used in the 022769 shot when compared with the MAST-U high-beta sample equilibrium, the corresponding aperture limited $k_{\perp}\rho_e$ range is larger for equivalent scattering radii, with a maximum $k_{\perp}\rho_e$ of 0.79 for

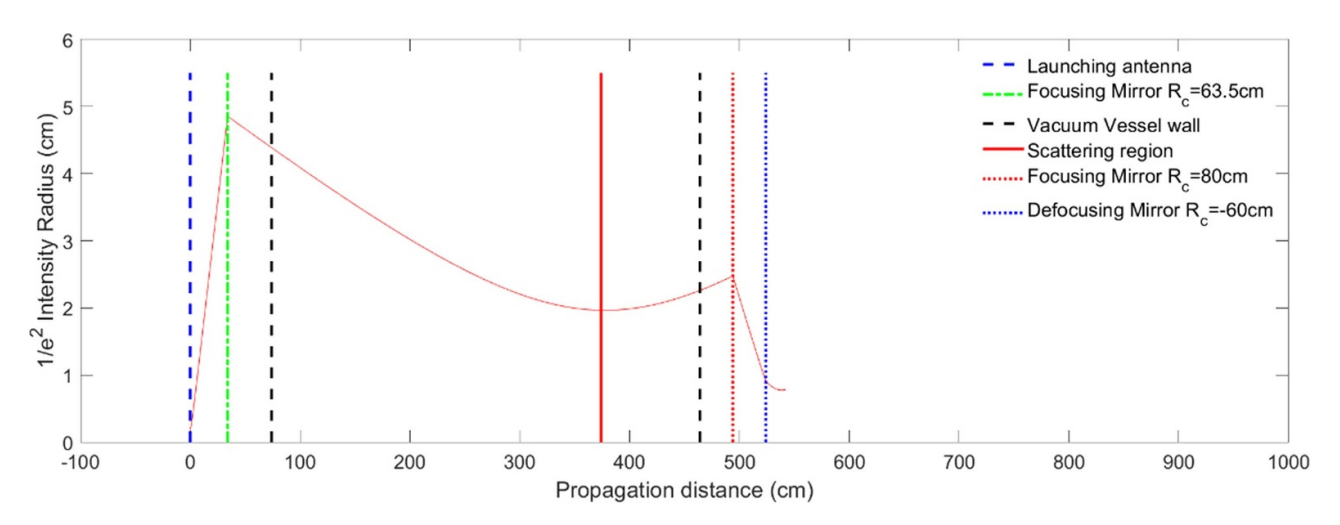


Figure 7. ABCD matrix calculations of Gaussian beam waist evolution for primary beam projected through launching and receiving optics and across the MAST-U vacuum vessel.

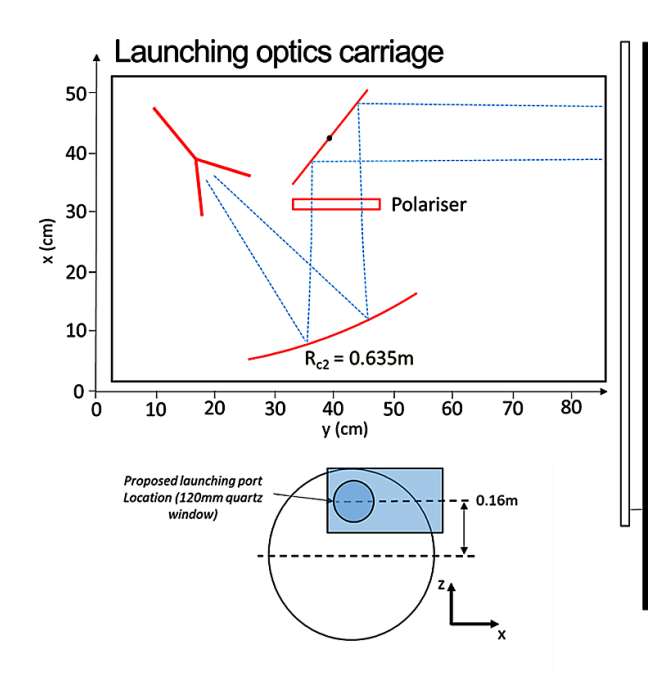


Figure 8. Illustration of launching optics carriage including launching antenna, focusing mirror, 2-axis adjustable redirecting mirror and rotatable linear polariser.

r/a=0.8 ($R_{scatt}=1.268$ m). Figures 12(a) and (b) shows the scattered signal power to noise ratio as a function of $k_{\perp}\rho_{e}$ for the MAST-U high-beta sample equilibrium and MAST 022769 shot respectively. These were calculated using the localisation data $L_{\rm FWHM}$ plotted in figures 10 and 11 substituted into equation (1) to compute the scattered power for a plane wave scattering off a coherent density fluctuation.

In both cases the signal to noise ratio drops to a minimum of around 10 for higher $k_{\perp}\rho_e$ values (larger scattering angles). In section 3.4, the scattered power due to a finite Gaussian beam incident on a simulated turbulence spectrum $\delta \hat{n}_e(\mathbf{k},\omega)$ is calculated using equation (2), providing realistic estimates for the power spectrum received on each channel of the instrument detector array.

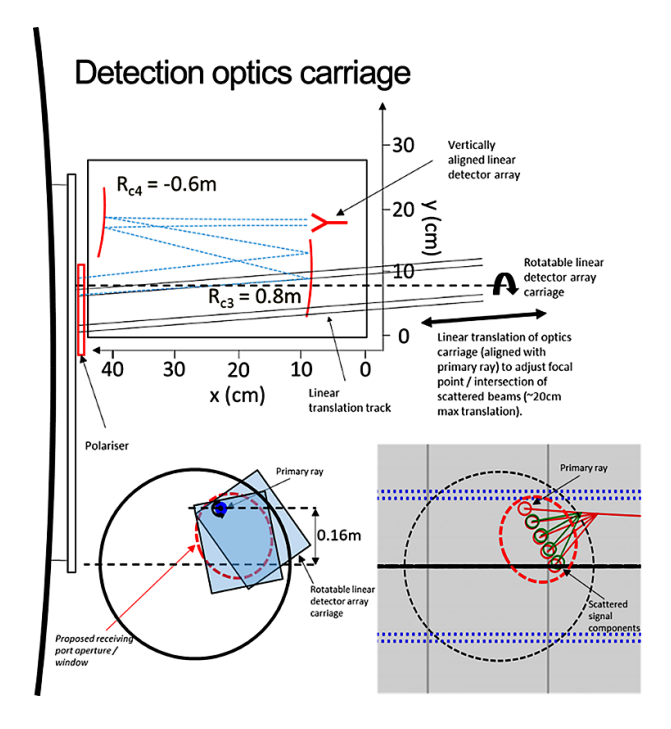


Figure 9. Illustration of receiving optics carriage including focussing/defocussing mirror pair, rotatable linear polariser and vertically aligned receiving antennae array.

Although the MAST-U high-k scattering diagnostic is primarily optimised to measure bi-normal aligned electron scale turbulence, due to the pitch rotation capabilities of the receiving carriage and focussing optics, it is possible to rotate the detector channels outside strictly bi-normal alignment and measure a combination of bi-normal k_b and normal k_n turbulence wavevectors on each channel from a given radial scattering coordinate. Figure 13 illustrates the scattered channel distributions corresponding to a bi-normal wavevector range of $k_b \rho_e = 0$ –0.63 and a normal wavevector range of $\pm k_n \rho_e = 0.52$. It is evident that some of the scattered components are outside the limits of the elliptical receiving window

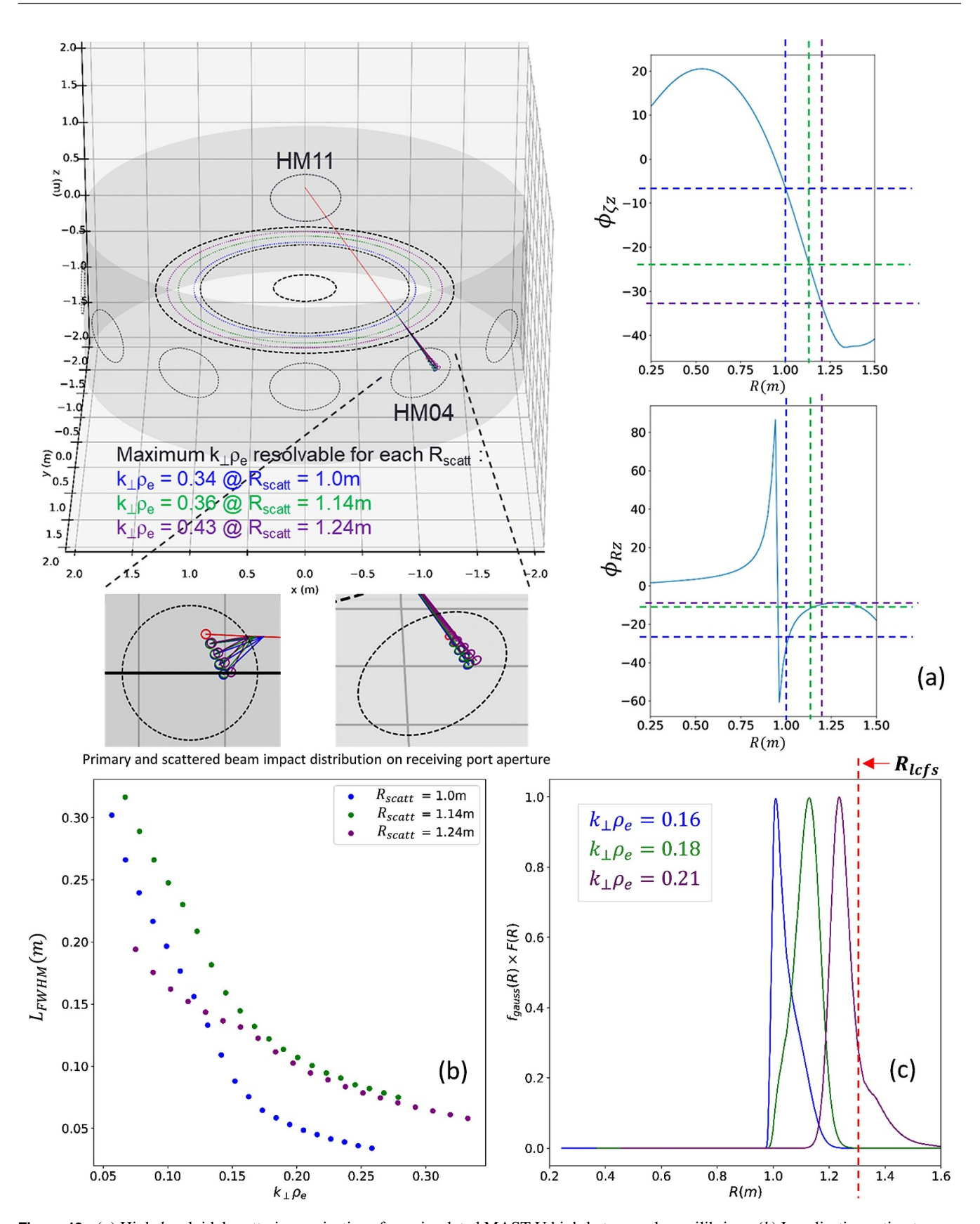


Figure 10. (a) High-k poloidal scattering projections for a simulated MAST-U high-beta sample equilibrium. (b) Localisation estimates as a function of $k_{\perp}\rho_{e}$ for three scattering radial coordinates corresponding to the FWHM of (c) the instrument selectivity functions.

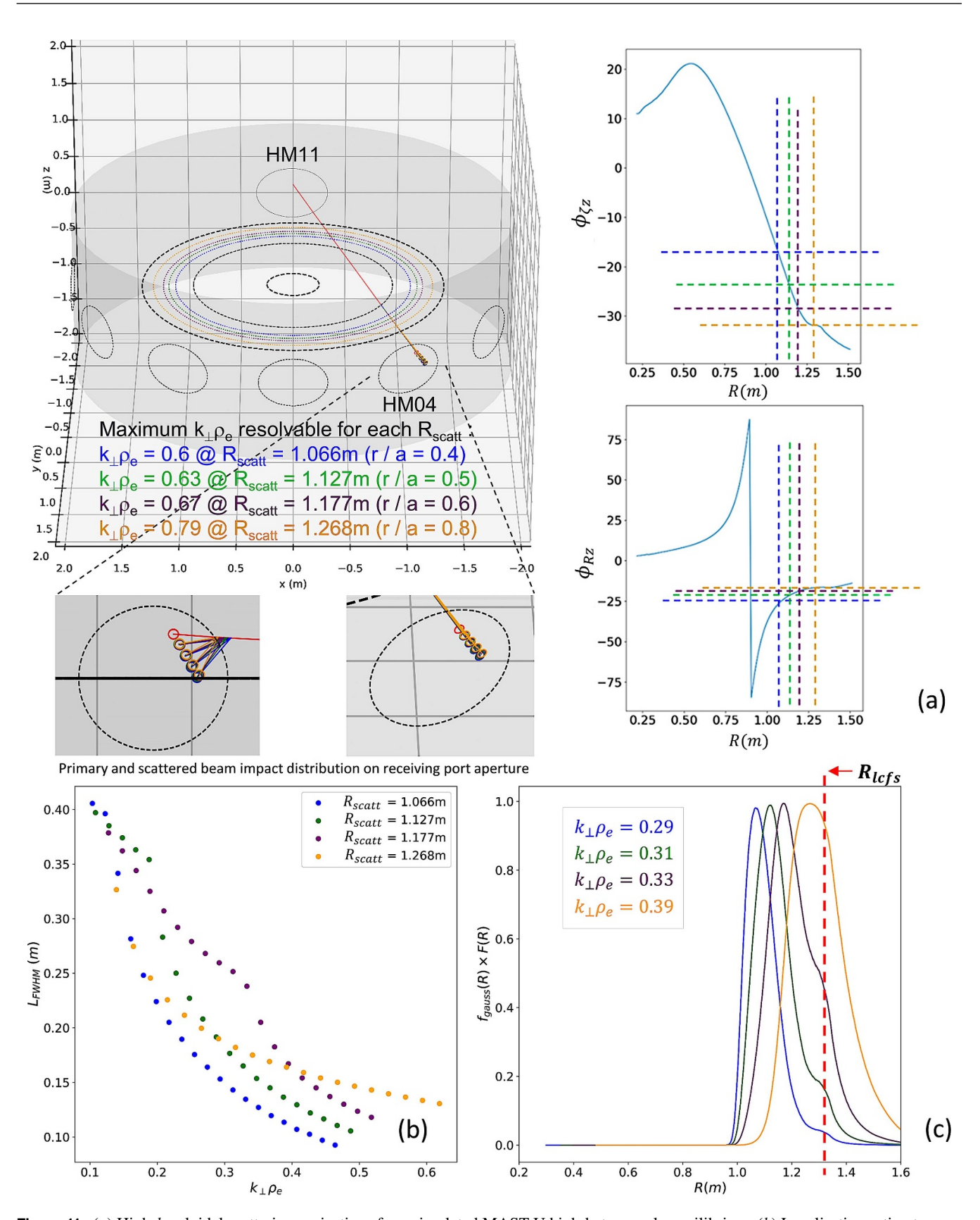


Figure 11. (a) High-k poloidal scattering projections for a simulated MAST-U high-beta sample equilibrium. (b) Localisation estimates as a function of $k_{\perp}\rho_{e}$ for three scattering radial coordinates corresponding to the FWHM of (c) the instrument selectivity functions.

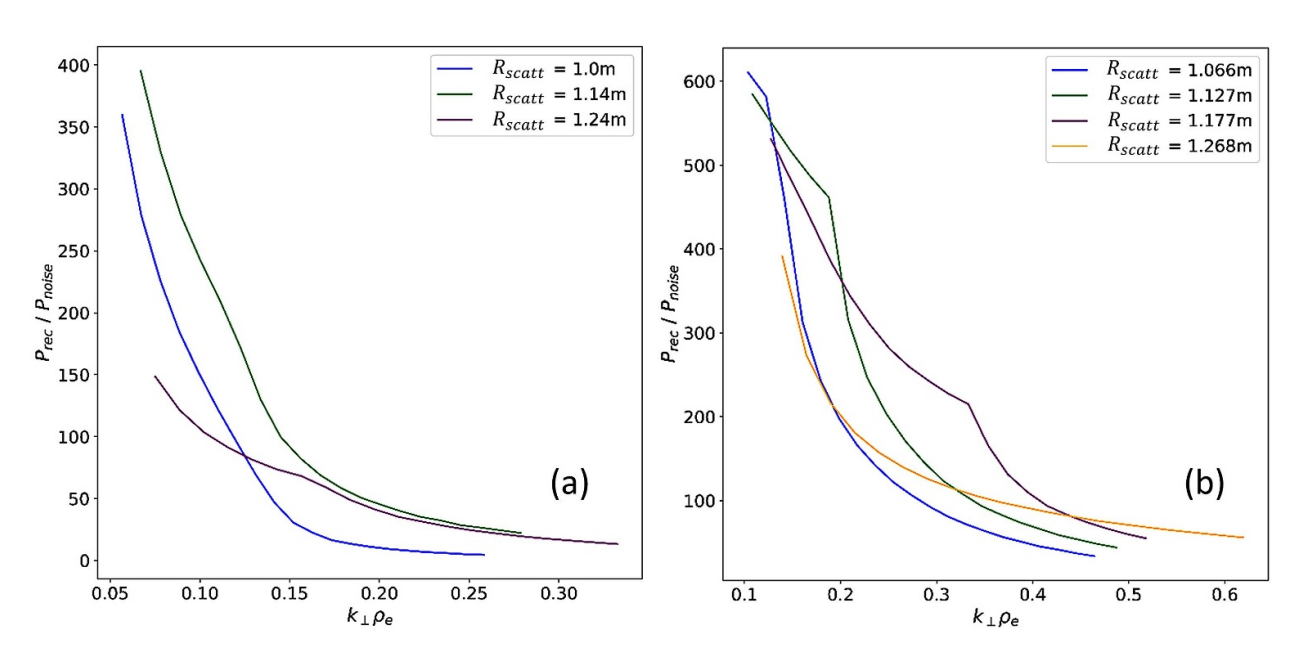


Figure 12. Received power to noise ratio for (a) the MAST-U sample high-beta equilibrium and (b) the MAST 022769 shot equilibrium using equation (1) and the localisation estimates L_{FWHM} in figures 9(b) and 10(b).

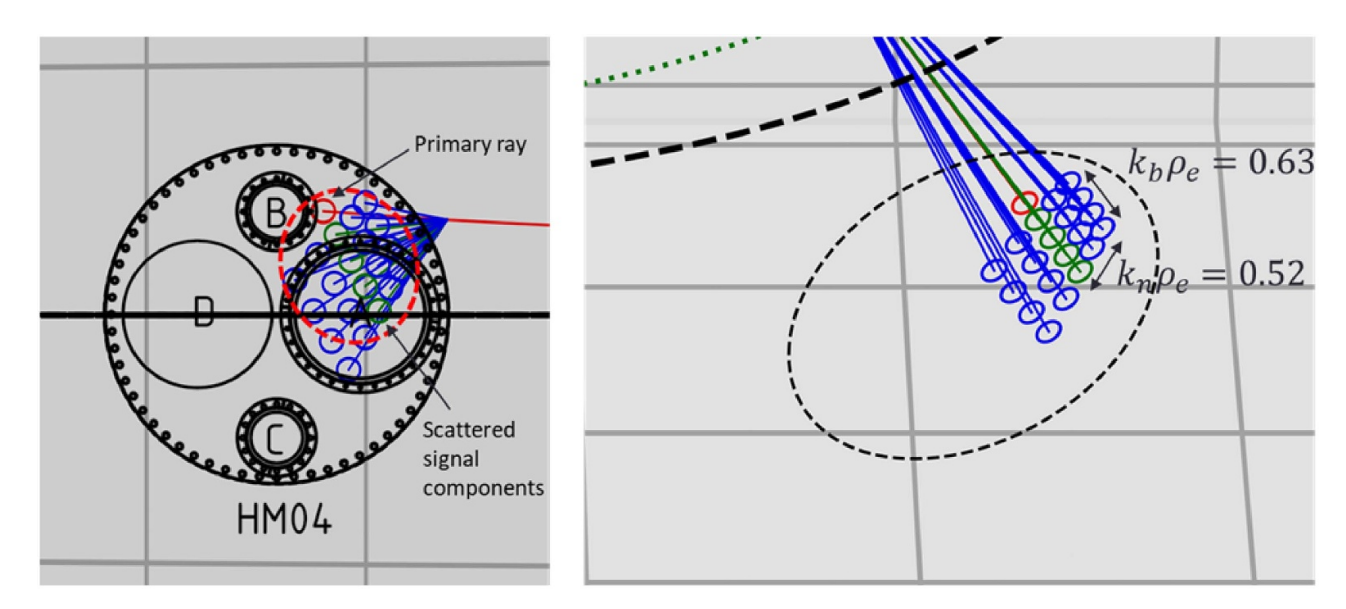


Figure 13. Projections of strictly bi-normal (green) and normal + bi-normal (blue) turbulence wavenumber contributions to scattered spectrum for $k_b = 3.95 \times 10^2$, 8.52×10^2 , 1.31×10^3 , 1.77×10^3 m⁻¹ (green) and $k_n = -1.5 \times 10^3$, -7.5×10^2 , 0.0,

aperture, however for appropriate carriage rotation, a significant portion are measurable. This further extends the measurement capabilities of the instrument in characterising the radially dependent electron scale turbulence spectrum, as will be further illustrated in section 3.4.

3.3. Electron scale gyrokinetic analysis of the reference MAST case

In this section, we describe electron scale gyrokinetic simulations used to provide realistic turbulence fluctuation maps used for synthetic diagnostic development in section 3.4. We

briefly describe the local (flux-tube) gyrokinetic simulations performed at different radial locations of the MAST reference case (shot 022769) using both kinetic ions and electrons. In particular, we consider four radial surfaces at r/a = 0.4, r/a = 0.5, r/a = 0.6, and r/a = 0.8. The choice of this MAST case is partially motivated by a previous gyrokinetic analysis of 022769 [40] that shows dominant transport from ETG turbulence at r/a = 0.5 and r/a = 0.6, which is comparable to the experimental heat flux value [39]. The gyrokinetic analysis [40] reveals the presence of an MTM (Microtearing Mode) ion scale instability at these surfaces in the bi-normal direction. This instability is neglected here however as the

Table 1. Miller parameterisation of the radial surface at $r/a \in \{0.4, 0.5, 0.6, 0.8\}$ of the MAST equilibrium shot 22769. The parameters listed are the safety factor q, the magnetic shear $\hat{s} = \frac{r}{q} \frac{dq}{dr}$, the elongation κ and its radial derivative κ' , the triangularity δ and its radial derivative δ' , the Shafranov shift Δ' , $\beta_e = 2 \mu_0 p_e/B_0^2$ (where p_e is the electron pressure). Also listed the local logarithmic radial gradient of electron density, electron temperature and ion temperature.

r/a	0.4	0.5	0.6	0.8
q	1.04	1.1	1.2	2.5
\hat{s}	0.06	0.34	1.1	4.63
κ	1.41	1.41	1.42	1.49
κ'	-0.02	0.04	0.16	0.53
δ	0.10	0.16	0.14	0.23
δ'	0.29	0.22	0.24	0.90
Δ'	-0.09	-0.13	-0.18	-0.35
eta_e	0.07	0.06	0.05	0.03
β'	-0.53	-0.57	-0.49	-0.29
a/L_{n_e}	0.4	0.2	0.3	0.06
a/L_{T_e}	1.6	2.1	2.2	3.1
a/L_{T_i}	1.3	1.7	2.0	3.7

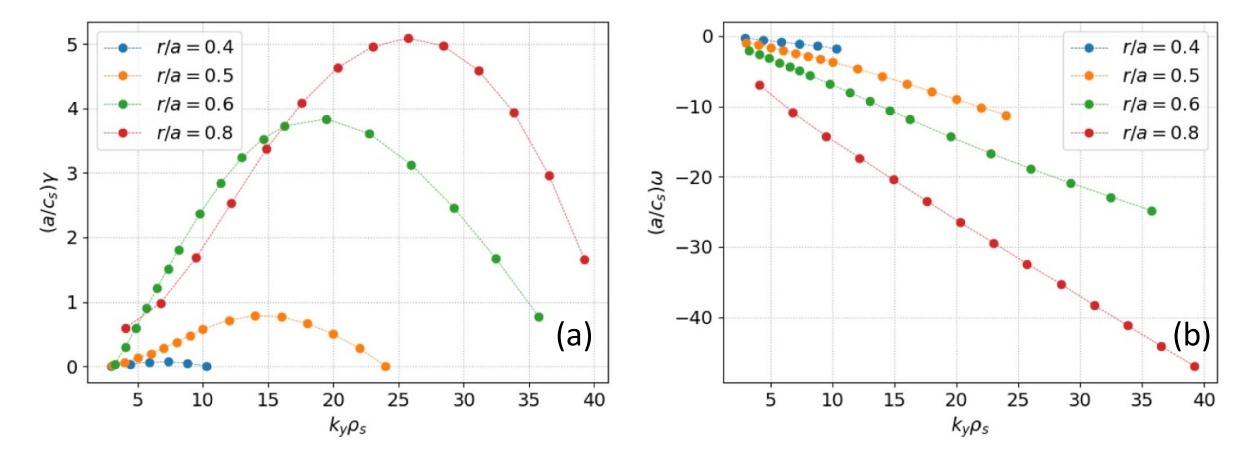


Figure 14. Growth rate (a) and mode frequency (b) of the electron scale instability as a function of the bi-normal wavevector $k_y \rho_s$ from linear gyrokinetic simulations at $r/a \in \{0.4, 0.5, 0.6, 0.8\}$. The growth rate and the mode frequency values are normalised to c_s/a evaluated on the corresponding radial surface.

proposed diagnostic has been optimised primarily for electron scale measurements in the bi-normal direction. MTMs do however have a very fine radial structure (high k_x), which may be detectable with the extended normal k_n measurement capabilities described in the previous section. The local linear and nonlinear gyrokinetic simulations considered in this work are performed using the CGYRO code [41]. The numerical resolution considered in linear simulations in the parallel, radial, velocity and pitch-angle direction is (n_{θ}, n_r, n_v) $n_{\mathcal{E}}$) = (32, 32, 10, 24), where the pitch-angle is defined as $\xi = v_{\parallel}/v$, with v_{\parallel} the velocity component parallel to the equilibrium magnetic field and v the total velocity. Two species, electrons and deuterium, are considered. Simulations are fully electromagnetic, i.e. they evolve electrostatic potential fluctuations, $\delta\phi$, as well as both perpendicular and parallel magnetic fluctuations, δA_{\parallel} and δB_{\parallel} . The value of local parameters obtained from a Miller parameterisation at each surface of the MAST 022769 shot [39], obtained using the Pyrokinetics Python library [42, 43] is reported in table 1. Further details on the equilibrium and profiles are detailed in M. Valovic *et al* [39].

Figure 14 shows the growth rate and mode frequency as a function of the wavevector component $k_y \rho_s$, where $\rho_s = c_s/\Omega_D$ is the sound ion Larmor radius, with $c_s = \sqrt{T_e/m_D}$, $\Omega_D =$ eB_0/m_D , T_e the electron temperature on the chosen radial surface, B_0 is the total magnetic field at the centre of the chosen flux surface, and m_D the deuterium mass. The growth rate and the mode frequency are normalised to c_s/a , evaluated on the corresponding radial surface. The maximum (normalised) growth rate value is achieved at r/a = 0.8, consistent with the higher ETG present at this location. A marginally stable ETG instability is found at r/a = 0.4. The frequency is negative (phase velocity in the electron diamagnetic direction) and proportional to k_v , as expected from ETG instability. The parallel mode structure of $\delta\phi$ and δA_{\parallel} at $k_{y}\rho_{s}\simeq16$ of the r/a = 0.5 surface is shown in figure 15. The amplitude of $e\delta\phi/T_e$ significantly exceeds that of $\delta A_{\parallel}/(\rho_s B_0)$, thus supporting the electrostatic nature of the underlying micro-instability.

The nonlinear simulations were performed with the numerical resolution $(n_{\theta}, n_{\nu}, n_{\xi}) = (32, 10, 24)$ considering a $k_{y}\rho_{s}$ range that covers the linear electron scale instability spectrum

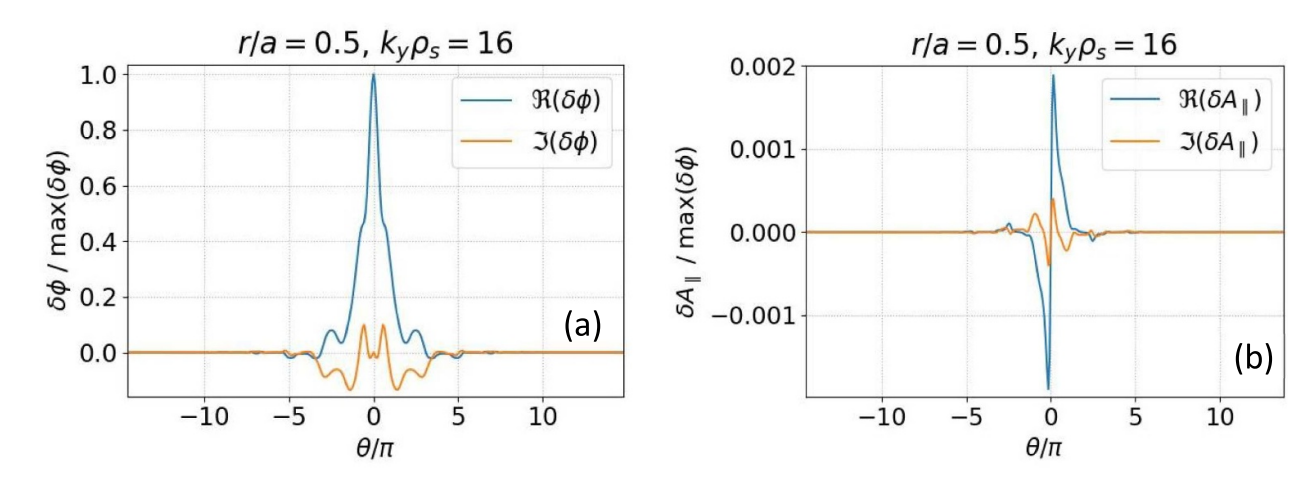


Figure 15. Parallel mode structure of $e\delta\phi/(\rho_*T_e)$ (a) and $\delta A_{\parallel}/(\rho_*\rho_s B_0)$ (b) corresponding to the $k_y\rho_s\simeq 26$ mode of the $r/a\simeq 0.5$ surface. Both $\delta\phi$ and δA_{\parallel} are normalised to max $\delta\phi$.

Table 2. Numerical resolution of the (k_x, k_y) grid used in the nonlinear simulations at different radial positions.

r/a	n_{k_y}	n_{k_x}	$\Delta k_y ho_s$	$\Delta k_x \rho_s$
0.4	32	128	1.5	0.56
0.5	16	128	2.0	1.1
0.6	16	64	2.3	1.9
0.8	32	128	2.5	0.76

in figure 14 (see table 2 for the numerical resolution used in k_y and k_x). The equilibrium flow shear is not included in these nonlinear simulations. Flow shear was included in previous GK simulations of ETG turbulence in MAST and had little impact on the electron-scale turbulence [23].

The saturated heat flux value (normalised to the local gyro-Bohm heat flux $Q_{\rm gB} = \rho_*^2 n_e T_e c_s$) obtained from the nonlinear simulations is shown in figure 16 as a function of the radial position. As expected from the linear analysis, the heat flux driven by the ETG instability increases with radius. Figure 16 shows also the relative density fluctuation amplitude from ETG turbulence at the outboard midplane as a function of radius.

$$\frac{\delta n_e}{n_e} = \frac{1}{n_e} \left\langle \sqrt{\sum_{k_x, k_y} \left| \delta n_e \left(k_x, k_y, \theta = 0, t \right) \right|^2} \right\rangle_T$$

where $\langle \cdot \rangle_T$ denotes the time average performed over the last 30% of the total simulation time. We note that the density fluctuation amplitude increases with radius, similarly to the heat flux. Figure 16 shows also a snapshot of the electron density fluctuations at the outboard midplane and r/a=0.5 taken at the last simulation time. The presence of radially elongated streamers is clearly visible in figure 16, thus revealing a strong anisotropy of the turbulence between the radial and bi-normal directions, discussed in more detailed in the following sections. This anisotropy is observed at all the radial locations considered in this work and is consistent with previous observations [23].

3.4. Synthetic high-k diagnostic for projecting high-k scattering measurements on MAST-U

The predicted density fluctuation spectra from the CGYRO electron scale gyrokinetic simulations are used to predict the measured scattered power spectra from the proposed high-*k* scattering system on MAST-U. A synthetic/numerical implementation of the proposed high-*k* diagnostic is used for this purpose. The synthetic diagnostic employed here has recently been implemented into the Pyrokinetics framework [42, 43]. Consistent with the Pyrokinetics framework, the synthetic high-*k* diagnostic code is independent of the gyrokinetic code used to generate the density fluctuation spectra.

The high-k synthetic diagnostic employed here introduces the dependence of the scattered power on the density fluctuation power spectrum and on the spatial resolution $L_{\rm FWHM}$. As we saw in section 2.1, the dependence on the spatial resolution is important, since the spatial resolution has explicit dependence on the measured k_{\perp} (see equation (3)). The dependence of the high-k measurement localisation function is normally characterised by $L \propto 1/k_{\perp}$, which was absent in the previous synthetic high-k diagnostic analyses upon which this work is built [44–46]. This dependence is important as it can directly affect the physical interpretation of the measurement, as discussed below.

The synthetic high-k diagnostic takes as input the measured wavevector \mathbf{k}_{\perp} and the spatial location of scattering. The second step is to run a nonlinear gyrokinetic simulation that adequately resolves the measured \mathbf{k}_{\perp} at the given

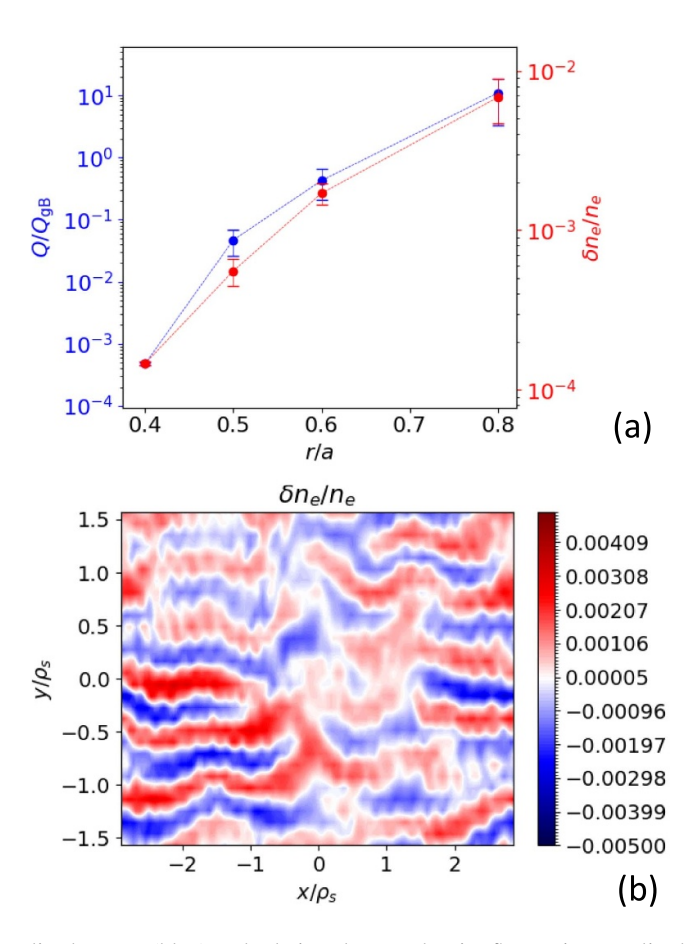


Figure 16. (a) Total heat flux normalised to $Q_{\rm gB}$ (blue) and relative electron density fluctuation amplitude at the outboard midplane (red) as a function of radius. (b) Snapshot of the electron density fluctuations at the outboard midplane taken at the last time step of the simulation at r/a = 0.5.

radial location of scattering. Therefore, it is a post-processing tool to the nonlinear gyrokinetic simulations that predicts the frequency and wavenumber spectrum given a set of selected scattered wavenumbers (here provided by Scotty [35]) and the simulated turbulence fluctuations. In what follows, we describe the implementation of the synthetic high-*k* diagnostic.

The starting point for developing the synthetic diagnostic is the Fourier expansion of the electron density fluctuation field δn_e generated by a local gyrokinetic code. In local gyrokinetics, fluctuating fields such as δn_e are represented as follows

$$\delta n_e(x, y, \theta, t) = \sum_{k_x, k_y} \delta \hat{n}_e(k_x, k_y, \theta, t) \exp(ik_x x + ik_y y)$$
 (7)

where k_x and k_y are the wavenumber components of \mathbf{k}_{\perp} as defined in Pyrokinetics, normalised by the reference magnetic field B_0 , and x and y are the respective conjugate spatial directions perpendicular to the background magnetic field vector \mathbf{B} . It is important to note that the internally defined k_x and k_y wavenumber components in gyrokinetic codes do not generally correspond to the normal and bi-normal components k_n and k_b . One needs a mapping between the two wavenumber definitions. In the synthetic high-k diagnostic, we map the selected k_n and k_b components obtained from Scotty to

the internal k_x and k_y components used in Pyrokinetics, as shown in recent works [46, 47]. This allows one to identify which wavenumber components k_x and k_y from a gyrokinetic code correspond to a specific diagnostic measurement configuration.

In addition to mapping the specific (k_n, k_b) pair to (k_x, k_y) , one needs to map the diagnostic wavenumber resolution Δk_{\perp} to Δk_x and Δk_y . The reader is referred to previous work [45] for additional details on the wavenumber mapping between (k_n, k_b) and (k_x, k_y) , as well as the corresponding wavenumber resolution. We note that, while the wavenumber components k_x and k_y are code dependent and not general, the k_n and k_b components remain universal, further justifying their use within the Pyrokinetics standardised framework for gyrokinetic simulations.

Simulated electron-scale turbulence from CGYRO is used in conjunction with a synthetic high-k diagnostic to enable quantitative projections of future high-k turbulence measurements in MAST-U. A specific example of four mapped wavenumber pairs (k_n, k_b) to (k_x, k_y) is given by the coloured dots on figure 17(a). These correspond to the four channels of the high-k scattering diagnostic for the radial location of r/a=0.5, and are overlayed to the 2D density fluctuation power spectrum $\langle |\delta \hat{n}_e|^2 (k_x, k_y) \rangle_T$ that has been numerically computed by CGYRO. The four channels are set in a

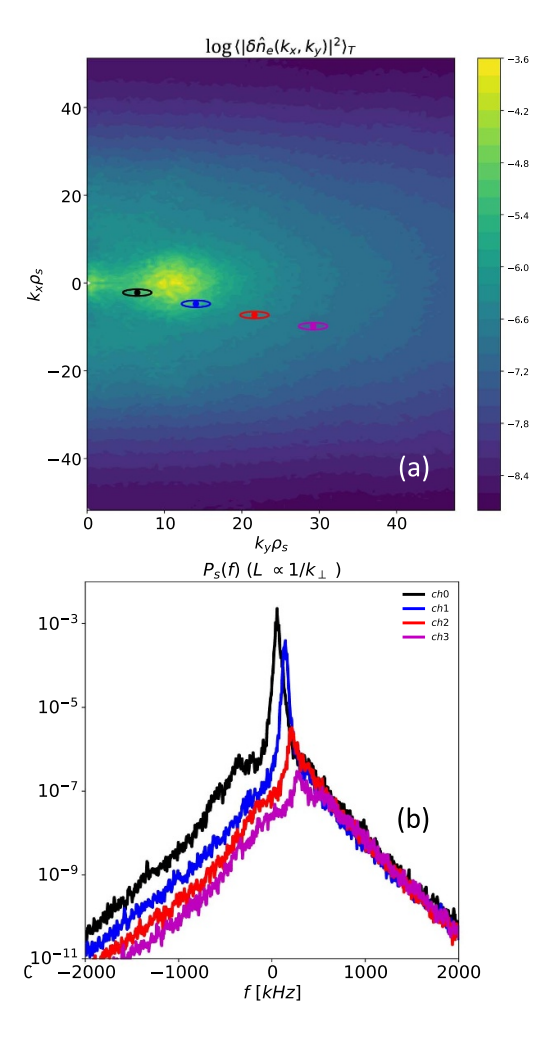


Figure 17. (a) Density fluctuation wavenumber power spectrum from the CGYRO simulation at r/a = 0.5, for a scattering configuration scanning the k_b component of the turbulence spectrum. Coloured dots and ellipses represent the selected \mathbf{k}_{\perp} and its resolution for the different channels on the scattering diagnostic, respectively. (b) Frequency spectrum of the turbulent electron density fluctuation power corresponding to the selected wavenumbers in (a).

configuration to scan the bi-normal k_b component of the turbulence, while maintaining a fixed $k_n = 0$. We refer to this configuration as a k_b -scan. Although $k_n = 0$ for the four channels, the flux surface geometry and out of midplane scattering location introduces a different k_x for each channel (see Ruiz Ruiz PPCF 2020/2022 for additional details [44, 46]). The wavenumber resolutions Δk_x and Δk_y are represented by the ellipses surrounding each coloured point in figure 17(a), and correspond to the $1/e^2$ power contributions to the scattered power.

Figure 17(a) shows that the currently proposed configuration of the high-k scattering instrument can probe the density fluctuation spectrum close to the peak of spectrum by performing a scan in the bi-normal component k_b of the turbulence. This spectral peak is generally attributed to radially elongated and poloidally thin turbulent structures known as streamers [20–22]. Figure 17(b) shows the frequency spectral power (in arbitrary units) of the turbulent density fluctuations

corresponding to each coloured point in figure 17(a). As expected, the higher wavenumber channels exhibit a decreasing fluctuation power. Additionally, note how the higher wavenumbers also exhibit a higher frequency f. This is due to the nature of the turbulent fluctuations, which exhibit a higher frequency for higher wavenumbers. This means that turbulent structures of smaller physical dimensions propagate faster than those of larger physical dimensions. The propagation of the turbulence fluctuations in the plasma frame propagation is also commonly denominated as the phase velocity, given by f/k. We note here that the frequency shift from figure 17(b)is not a Doppler shift, as the Doppler shift is not included in the current analysis. Adding a Doppler shift to figure 17(b)would increase the frequency response required of the diagnostic, but would have no impact on the measured k_{\perp} nor on the total scattered power. Figure 17(b) could be quantitatively compared to experimental measurements from the high-k scattering instrument.

Figure 18 shows the predicted measurement range of the proposed diagnostic by performing a scan in the normal component k_n of the turbulence. We refer to this configuration as a k_n -scan. This measurement configuration is designed to select a finite $k_n = 8.78 \text{ cm}^{-1}$ that is close to the driving, or injection scale of the turbulence, which is also where ETG streamers are predicted to exist. The scattering configuration to perform a k_n -scan requires consideration of the physical diagnostic configuration. In the proposed high-k scattering instrument, a k_n scan is made possible by rotating the frame of detectors from strictly bi-normal alignment with a finite offset angle. Each channel of the linear detector array will then align with a unique combination of k_b and k_n values for a given scattering radius. As can be seen from figure 18, the scattering configuration of the diagnostic required to perform a k_n -scan predicts the measurement of the k_x dependence of the electron density fluctuation spectrum around the spectral peak due to ETG streamers. Taken together, figures 17 and 18 indicate that the MAST-U high-k scattering diagnostic will be successful at measuring both the k_x and the k_y dependence of the density fluctuation spectrum around the peak wavenumber of the radial streamers.

Despite the apparent limitation to four channels, the measurement could be populated with additional points corresponding to different *k*-values measured over repeated plasma discharges via collective linear translation of the Schottky diode detector array and discrete receiving antennae.

The frequency response of the turbulence for the k_n -scan configuration is given in figure 18(b). Note how the frequency dependence of the turbulent spectrum exhibits a similar dependence for the different selected k_n . Contrary to figure 17(b), where a clear shift of the frequency spectrum while scanning k_b is observable, figure 18(b) does not show a shift towards larger frequencies when scanning k_n . This is because the dominant contribution to the phase velocity of the turbulence is in the bi-normal direction, along k_b . Turbulent structures tend to propagate within the flux surface in the bi-normal direction much faster than in the radial direction, as confirmed by nonlinear gyrokinetic simulations [41, 48]. Figure 18(b) shows the expected clear dependence of the total

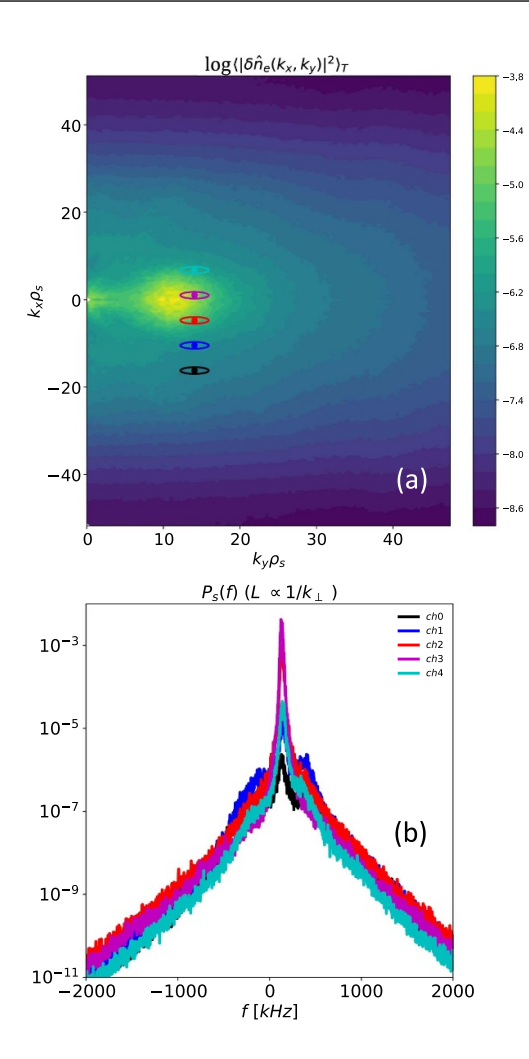


Figure 18. Similar to figure 17, this time performing a scan in the k_n component of the turbulence spectrum. (a) Density fluctuation wavenumber power spectrum from the CGYRO simulation at r/a = 0.5. (b) Frequency spectrum of the turbulent electron density fluctuation power corresponding to the selected wavenumbers in (a).

spectral amplitude in the frequency power spectrum. This dependence proved beneficial in the development and interpretation of figure 19.

A measurement of the total predicted scattered power and the corresponding electron density fluctuation power can also be performed by using the diagnostic. Figure 19(a) shows the total, synthetic scattered power $P_{\rm syn}$ as a function of the selected k_\perp from the proposed diagnostic for the k_b -scan configuration. The scattered power varies by several orders of magnitude with minor radius, as well as with the selected k_\perp . This large variation is primarily due to the variation of the turbulence fluctuation intensity with minor radius, which depends strongly on the gradients of the background plasma profiles, especially on the ETG as is visible in figure 14. Figure 19(b) shows the predicted electron density fluctuation power spectrum $\left< |\delta \hat{n}_e|^2 \left(k_\perp\right)/n_e^2 \right>_T$ as a function of $k_y \rho_s$ for the k_b -scan. Following equation (2), the measured electron density fluctuation spectrum can be inferred from the synthetic scattered power $P_{\rm syn}$ by $\left< |\delta \hat{n}_e|^2 \left(k_\perp\right)/n_e^2 \right>_T \propto k_\perp^2 P_{\rm syn}$, where the additional factor of k_\perp^2 has its origin in the k_\perp dependence of the

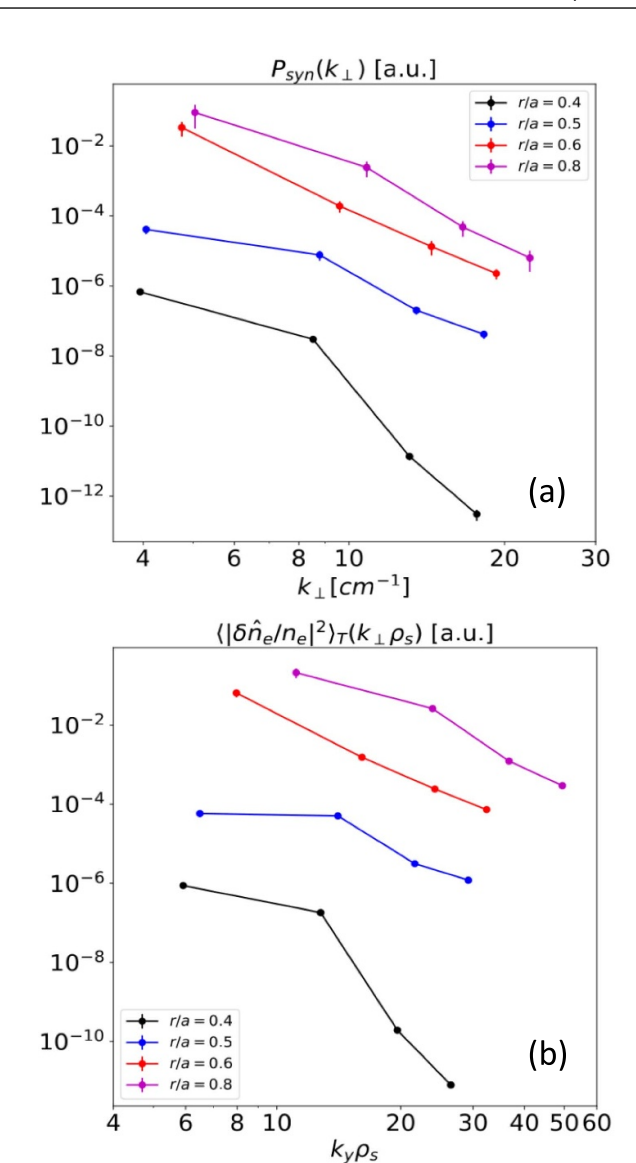


Figure 19. (a) Synthetic, predicted scattered power by high-k synthetic diagnostic and (b) electron density fluctuation power spectrum. A scan in the bi-normal k_b component of the turbulence was performed for r/a = 0.4, 0.5, 0.6 and 0.8. The large variation of the scattered power is due to the variation of the turbulence intensity with minor radius (see figure 16).

diagnostic spatial resolution L, see equation (2). Note how the peak $\left\langle \left| \delta \hat{n}_e \right|^2 (k_\perp) / n_e^2 \right\rangle_T$ around $k_y \rho_s \approx 10$ can be inferred for the radial location r/a = 0.5 (blue curve in figure 19(b), corresponding to figures 17 and 18). For larger $k_y \rho_s$, we observe a decrease in the spectral power with wavenumber, characteristic of the inertial range of the turbulent cascade. This behaviour is not observed at all radial locations, and would need to be analysed in detail on a case-by-case basis.

In addition to calculating the peak wavenumber k_b (or $k_y \rho_s$) corresponding to ETG streamers, the aspect ratio (k_y/k_x) of the turbulent eddies could also be calculated from such a measurement. Having measured $\left< |\delta \hat{n}_e|^2 \left(k_\perp\right)/n_e^2 \right>_T$, one could calculate the $1/e^2$ spectral widths w_{k_x} and w_{k_y} that characterise the spectral decay of the turbulent spectrum, respectively in the

 k_x and in the k_y directions. The aspect ratio of the turbulent eddies in the perpendicular direction to the background magnetic field can be calculated by the ratio of the radial correlation length to the bi-normal correlation lengths, which can in turn be related to the spectral widths as follows $l_r/l_b \approx w_{k_y}/w_{k_x}$ [45, 46]. This analysis is not the object of this publication, and its implementation is left to the analysis of data from a future measurement using the proposed high-k scattering instrument. Figure 19 suggests that the diagnostic will be able to quantitatively distinguish from conditions of strong and weak ETG turbulence drive in MAST-U, as well as to determine intrinsic characteristics of the turbulence, which is one of the main objectives of the diagnostic.

4. Discussion

A high-k electron scale turbulence scattering diagnostic model has been designed for future implementation on MAST-U. The instrument operates in a collective scattering regime $(1/k_{\perp}\lambda_{De} \geqslant 1)$ based on the principles of Bragg scattering, and is primarily designed to diagnose the ETG turbulence wavenumber spectrum in the bi-normal direction with adjustable spatial localisation from the plasma core to the edge pedestal region. Due to an operating frequency of 376 GHz, measurement within the core plasma is possible under all operational conditions of MAST-U. A highly flexible rotatable and translatable receiving optics carriage containing four scattering detector channels enables precise alignment with the bi-normal direction to be maintained whilst adjusting the radial location (and imaging focus) of the receiving optics. Rotational adjustment also facilitates measurement of a range of bi-normal k_b and normal k_n turbulence wavenumber combinations through rotational misalignment from strictly binormal incidence. For a sample high-beta MAST-U equilibrium, beam tracing simulations project the maximum normalised bi-normal wavenumber of measurement to be $k_{\perp}\rho_{e}\sim$ 0.34 in the core and $k_{\perp}\rho_{e}\sim0.43$ near the pedestal. For the reconstructed MAST shot 022769 with lower magnetic field, the maximum normalised bi-normal wavenumber of measurement is $k_{\perp}\rho_{e} \sim 0.6$ in the core and $k_{\perp}\rho_{e} \sim 0.79$ near the pedestal (these projections are aperture limited by the 250 mm × 290 mm elliptical receiving window). The instrument selectivity function along the path of scattering has been analysed using the formalism developed in section 2.1. This analysis combines the finite overlap of the incident and scattered Gaussian beams [37] with the rotational misalignment effect due to magnetic field pitch angle variation with radius [30, 36]. For the high-beta MAST-U equilibrium, the associated localisation length LFWHM varies between a maximum of ~ 0.33 m for $k_{\perp} \rho_e \sim 0.05$ in the core and a minimum of \sim 0.05 m for $k_{\perp}\rho_{e} > 0.25$ at all radial coordinates. For the 022769 MAST equilibrium, $L_{\rm FWHM}$ ranges from \sim 0.4 m in the core for $k_{\perp}\rho_{e}\sim0.1$ to ~0.08 m for $k_{\perp}\rho_{e}>0.45$. The localisation lengths have been used to estimate the scattered power assuming a single coherent density fluctuation with $dn_e/n_e \sim$ 4×10^{-6} . This yielded a maximum received power to detector noise ratio $P_{\rm rec}/P_{\rm noise}$ of $\sim 400 \to 600$ for both sample equilibria at smallest $k_\perp \rho_e$ and a $P_{\rm rec}/P_{\rm noise}$ of ~ 10 at maximum $k_\perp \rho_e$. The minimum scattered power is therefore comfortably above a reasonable detection threshold.

In order to compare the measurement specifications of the diagnostic with a sample ETG dominated turbulence map at corresponding radial scattering coordinates, electron scale localised (flux-tube) gyrokinetic simulations were conducted using the CGYRO code for the 022769 MAST equilibrium. The simulations are fully electromagnetic and use two species, electrons and deuterium ions. Calculations of the ETG turbulence linear growth rate [40] show a maximum (normalised) growth rate value at r/a = 0.8, consistent with the higher ETG at this radius. The correspondingly largest normalised turbulence wavenumber for peak growth is $k_v \rho_s = 26$ also occurring at r/a = 0.8. Only a marginal ETG instability is found at r/a = 0.4 with correspondingly lowest growth rate and lowest turbulence wavenumber for peak growth at $k_v \rho_s = 7$. The nonlinear gyrokinetic simulations were conducted for r/a = 0.4, 0.5, 0.6 and 0.8 using a $k_v \rho_s$ range determined by the electron scale instability spectrum from the linear calculations. As expected, the heat flux driven by the ETG instability increases with radius as does the relative amplitude of the density fluctuations, with dn_e/n_e ranging between $\sim 1 \times 10^{-4}$ in the core to $\sim 1 \times 10^{-2}$ at the pedestal. This is at least 25× greater than the $\delta n_e/n_e = 4 \times 10^{-6}$ used in the scattered power calculations, equating to a received power that is 625× greater than previous minimum estimates.

In order to properly scale and project the measured normalised turbulence wavenumber specifications of the high-k scattering diagnostic to CGYRO ETG turbulence maps, a synthetic diagnostic framework was used [44]. This framework has been implemented within the Pyrokinetics Python library [42, 43] and enables calibration of the measured wavenumber specifications into gyrokinetic field-aligned coordinates, accounting for the plasma elongation and Shafranov shift [44]. The synthetic diagnostic framework also enables calculation of the scattered power frequency spectrum for each channel of the scattering diagnostic, using the wavenumber specifications and localisation lengths derived from ray-tracing to enable quantitative projections of future high-k turbulence measurements on MAST-U. Wavenumber coordinate mapping between the scattering instrument projections and CGYRO for each of the radial coordinates shows that the lowest 2 channels in $k_{\perp}\rho_{e}$ are coincident with the peaks in the turbulence spectra in all cases. This indicates that the $k_{\perp}\rho_e$ range measurable by the proposed high-k diagnostic would be more than adequate to resolve the simulated turbulence spectra, whilst providing additional channels for extended wavenumber coverage and relative measurements at lower expected powers. The additional channels can also facilitate off-bi-normal rotational misalignment for measurements combining bi-normal and normal turbulence wavenumber contributions. The composite synthetic power spectra illustrate that variations in the scattered power received per channel and for different r/a values are

clearly discernible, allowing mapping of the electron scale turbulence spectra both by wavenumber and spatial coordinate. The diagnostic will therefore be able to quantitatively distinguish between conditions of strong and weak ETG turbulence on MAST-U, whilst providing intrinsic characteristics of the turbulence at spatial coordinates from the core to the pedestal.

5. Conclusions

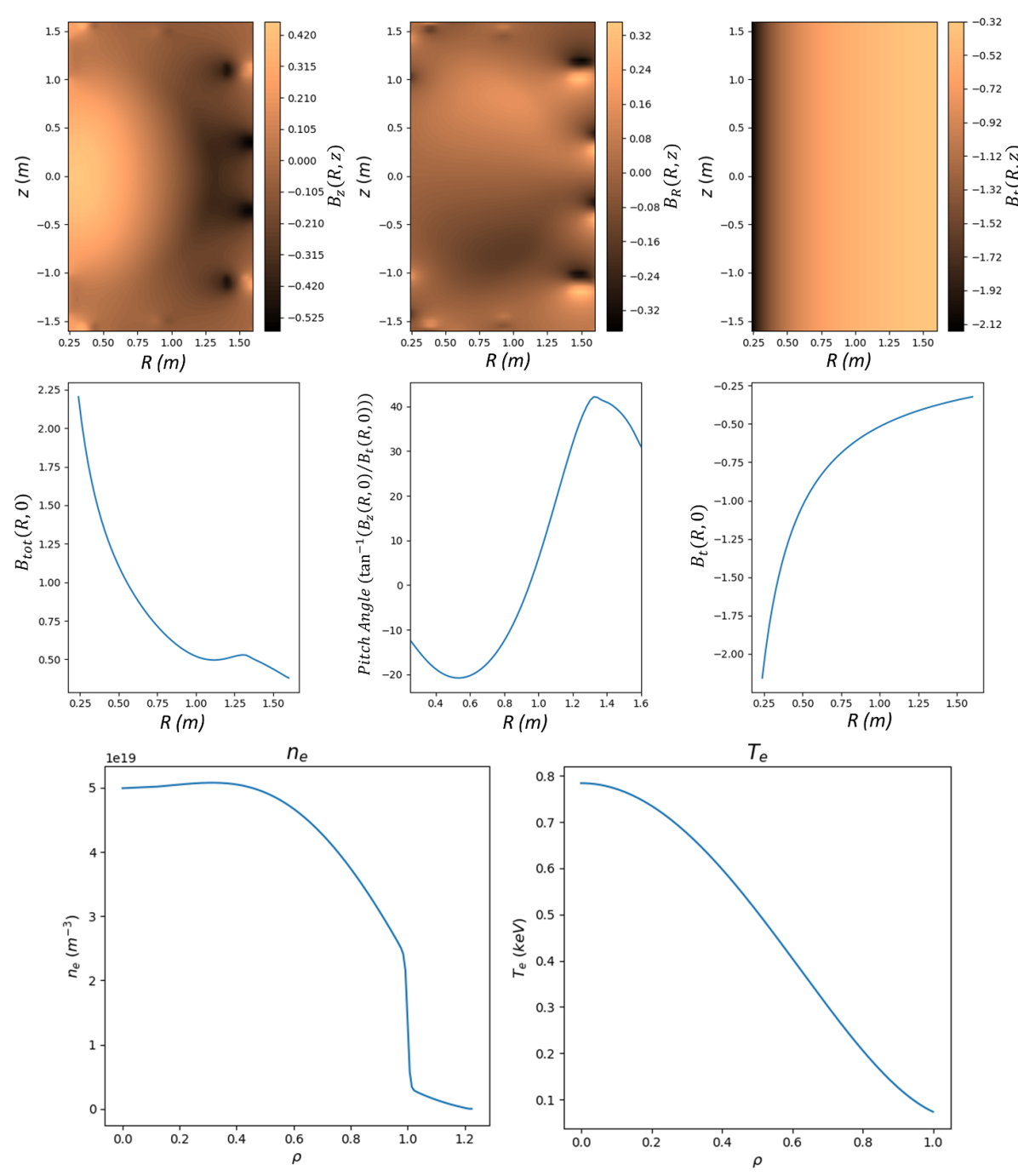
We have used a synthetic diagnostic approach to design a highly optimised yet flexible electron-scale turbulence diagnostic, using powerful modelling tools to predict the sensitivity and spectral range of measurement whilst diagnosing both normal and bi-normal turbulence wavenumbers. The morphology of the spherical tokamak plasma (notable, the magnetic field pitch rotation with radius) enhances the localisation of measurement and provides further motivation for applying this instrument to MAST-U plasmas. There is however no reason why the same numerical optimisation and analysis technique could not be applied to a conventional tokamak. The proposed diagnostic opens up opportunities to study new regimes of turbulence and confinement, particularly in association with upcoming non-inductive, microwave based current drive experiments on MAST-U. These experiments are critical to the development of the future STEP (Spherical Tokamak for Energy Production) reactor and operational parameters. On MAST-U, the diagnostic expands on the capabilities of existing DBS diagnostics both in terms of turbulence wavenumber measurement range and core plasma access, while complementing ion-scale measurements of the BES diagnostic. It is also of particular relevance to the future STEP reactor due to its high operational frequency and resilient component design, making it highly suited to operation during burning plasma experiments where high-power microwaves are used for heating and current drive. Target physics problems include the diagnosis of ETG turbulence anisotropy/streamer formation, identifying cross-scale turbulence effects such as the suppression of electron-scale turbulence by ion-scale eddies [9] and the study of ETG turbulence in the presence of large scale (MHD) fluctuations (as expected in high-beta spherical tokamak plasmas) and Alfvénic instabilities which can themselves be destabilised by highly energetic particles (such as alpha particles) during future burning plasma experiments on STEP. The initial measurements of these effects on MAST-U will help benchmark the predictions of numerical models, and serve as a baseline for future comparative measurements of STEP turbulence [49, 50].

Acknowledgment

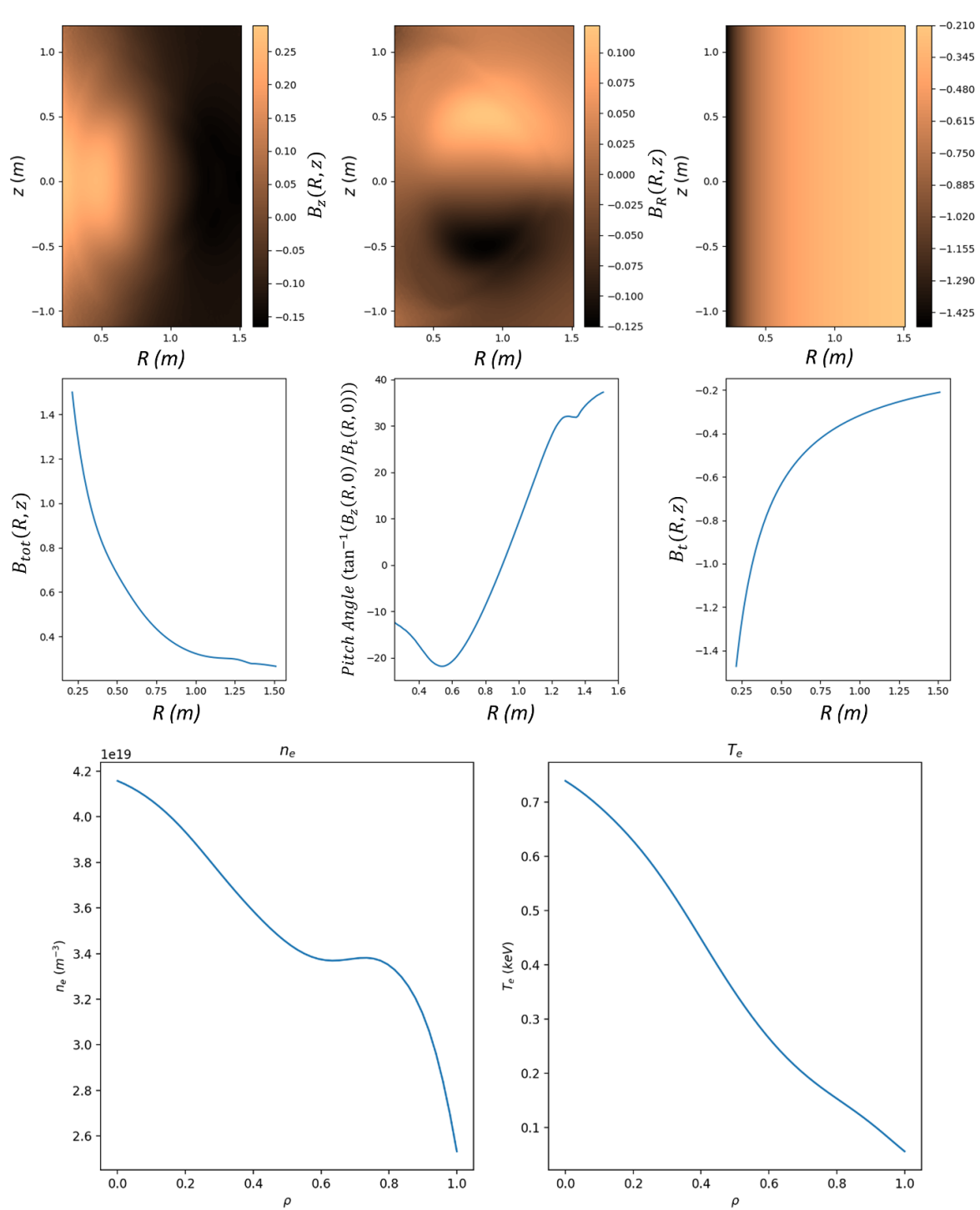
The authors are grateful for productive discussions with T.L. Rhodes at UCLA in the development of this work. The authors would also like to thank J. Harrison, R. Scannell and K. Hawkins at CCFE for their valuable input. The research was made possible by funding received from the EPSRC (Grant No. EP/R034737/1) and from A*STAR, via Green Seed Fund C231718014 and a SERC Central Research Fund. This work has been partially funded by the EPSRC Energy Programme (Grant No. EP/W006839/1). J. Ruiz-Ruiz was partially funded by EPSRC Grant EP/W026341/1.

Appendix

MAST-U High-beta sample equilibrium



MAST 022769 shot equilibrium



ORCID iDs

D.C. Speirs https://orcid.org/0000-0001-5705-6126
J. Ruiz Ruiz https://orcid.org/0000-0003-4258-5273
M. Giacomin https://orcid.org/0000-0003-2821-2008
V.H. Hall-Chen https://orcid.org/0000-0001-6009-3649
R. Vann https://orcid.org/0000-0002-3105-2546
A. Field https://orcid.org/0000-0003-0671-9668

References

- [1] Wilson H. 2019 Phil. Trans. R. Soc. A377 20170435
- [2] Harrison J.R. et al 2019 Nucl. Fusion 59 112011
- [3] Kaye S.M., Connor J.W. and Roach C.M. 2021 Plasma Phys. Control. Fusion 63 123001
- [4] Fuchs V., Harten L. and Bers A. 1980 Nucl. Fusion 20 630-5
- [5] Kikuchi M. and Azumi M. 2015 Frontiers in Fusion Research II: Introduction to Modern Tokamak Physics vol 7 (Springer) pp 175–227
- [6] Li P.-Y., Hatch D.R., Chapman-Oplopoiou B., Saarelma S., Roach C.M., Kotschenreuther M., Mahajan S.M. and Merlo G. 2024 Nucl. Fusion 64 016040
- [7] Masui H., Ishizawa A., Imadera K., Kishimoto Y. and Nakamura Y. 2022 Nucl. Fusion 62 074001
- [8] Giacomin M. and Ricci P. 2022 Phys. Plasmas 29 062303
- [9] Maeyama S., Idomura Y., Watanabe T.-H., Nakata M., Yagi M., Miyato N., Ishizawa A. and Nunami M. 2015 Phys. Rev. Lett. 114 255002
- [10] Maeyama S., Watanabe T.-H., Idomura Y., Nakata M., Ishizawa A. and Nunami M. 2017 Nucl. Fusion 57 066036
- [11] Costley A.E. 2019 Phil. Trans. R. Soc. A 377 20170439
- [12] Howard N.T., Holland C., White A.E., Greenwald M., Candy J. and Creely A.J. 2016 Phys. Plasmas 23 056109
- [13] Snipes A. et al 2021 Nucl. Fusion 61 106036
- [14] Zhuang G. et al 2019 Nucl. Fusion 59 112010
- [15] Sorbom B.N. et al 2015 Fusion Eng. Des. 100 378-405
- [16] Gibney E. 2019 *Nature* (https://doi.org/10.1038/d41586-019-03039-9)
- [17] Field A.R., Dunai D., Gaffka R., Ghim Y.-C., Kiss I., Mészáros B., Krizsanóczi T., Shibaev S. and Zoletnik S. 2012 Rev. Sci. Instrum. 83 013508
- [18] Rhodes T.L. et al 2022 Rev. Sci. Instrum. 93 113549
- [19] Shi P., Scannell R., Wen J., Shi Z.B., Michael C., Rhodes T., Hall-Chen V.H., Yang Z.C., Jiang M. and Zhong W.L. 2023 J. Instrum. 18 C11022
- [20] Drake J.F., Guzdar P.N. and Hassam A.B. 1988 Phys. Rev. Lett. 61 2205–8
- [21] Dorland W., Jenko F., Kotschenreuther M. and Rogers B.N. 2000 Phys. Rev. Lett. 85 5579
- [22] Jenko F., Dorland W., Kotschenreuther M. and Rogers B.N. 2000 Phys. Plasmas 7 1904

- [23] Roach C.M. *et al* 2009 *Plasma Phys. Control. Fusion* **51** 124020
- [24] Webster H. et al 2023 EPJ Web Conf. 277 04004
- [25] Smith D.R., Mazzucato E., Lee W., Park H.K., Domier C.W. and Luhmann N.C. 2008 Rev. Sci. Instrum. 79 123501
- [26] Smith D.R. et al 2009 Phys. Rev. Lett. 102 225005
- [27] Barchfeld R. et al 2018 Rev. Sci. Instrum. 89 10C114
- [28] Catto P.J. 1978 Plasma Phys. 20 719
- [29] Frieman E. and Chen L. 1982 Phys. Fluids 25 502-8
- [30] Devynck P., Garbet X., Laviron C., Payan J., Saha S.K., Gervais F., Hennequin P., Quemeneur A. and Truc A. 1993 Plasma Phys. Control. Fusion 35 63
- [31] Mazzucato E. 2014 Electromagnetic Waves for Thermonuclear Fusion Research (World Scientific Publishing)
- [32] Mazzucato E. 2003 Phys. Plasmas 10 753
- [33] Hall-Chen V.H. et al 2022 arXiv:2211.17141
- [34] Hall-Chen V.H. et al 2022 Rev. Sci. Instrum. 93 103536
- [35] Hall-Chen V.H., Parra F.I. and Hillesheim J.C. 2022 *Plasma Phys. Control. Fusion* **64** 095002
- [36] Mazzucato E. 2006 Plasma Phys. Control. Fusion 48 1749
- [37] Bindslev H., Meo F. and Korsholm S.B. 2003 ITER fast ion collective Thomson scattering: feasibility study (Risø National Laboratory)
- [38] Bélanger P.A. 1991 Opt. Lett. 16 196-8
- [39] Valovič M. et al 2011 Nucl. Fusion 51 073045
- [40] Giacomin M., Dickinson D., Kennedy D., Patel B.S. and Roach C.M. 2023 Plasma Phys. Control. Fusion 65 095019
- [41] Candy J., Belli E.A. and Bravenec R.V. 2016 *J. Comput. Phys.* **324** 73–93
- [42] Patel B.S. *et al* 2022 Pyrokinetics (version 0.4.0) (available at: https://github.com/pyro-kinetics/pyrokinetics)
- [43] Patel B.S. et al 2024 J. Open Source Softw. 9 5866
- [44] Ruiz Ruiz J., Guttenfelder W., White A.E., Howard N.T., Candy J., Ren Y., Smith D.R. and Holland C. 2020 Plasma Phys. Control. Fusion 62 075001
- [45] Ruiz Ruiz J., Guttenfelder W., White A.E., Howard N.T., Candy J., Ren Y., Smith D.R., Loureiro N.F., Holland C. and Domier C.W. 2019 Plasma Phys. Control. Fusion 61 115015
- [46] Ruiz Ruiz J. et al 2022 Plasma Phys. Control. Fusion 64 055019
- [47] Pratt Q. et al 2024 Nucl. Fusion 64 016001
- [48] Ruiz Ruiz J., Guttenfelder W., White A.E., Howard N.T., Candy J., Ren Y., Smith D.R., Loureiro N.F., Holland C. and Domier C.W. 2020 Phys. Plasmas 27 122505
- [49] Kennedy D., Giacomin M., Casson F.J., Dickinson D., Hornsby W.A., Patel B.S. and Roach C.M. 2023 Nucl. Fusion 63 126061
- [50] Giacomin M., Kennedy D., Casson F.J., Ajay C.J., Dickinson D., Patel B.S. and Roach C.M. 2024 Plasma Phys. Control. Fusion 66 055010